DELIVERY AND ACTUATION OF COLLOIDAL MICROBOTS IN THREE DIMENSIONAL MICROENVIRONMENTS FOR BIOMEDICAL APPLICATIONS

by

Coy Zimmermann

A thesis submitted to the Faculty and the Board of Trustees of the Colorado School of Mines in partial fulfillment of the requirements for the degree of Doctor of Philosophy (Chemical Engineering).

Golden, Colorado

Date _____

Signed: _____

Coy Zimmermann

Signed: _____

Dr. David W. M. Marr
Thesis Advisor

Golden, Colorado

Date _____

Signed: _____

Daniel Knauss
Interim Department Head
Chemical and Biological Engineering

ABSTRACT

Microbots are an exciting emerging biomedical technology where micro-scale "bots" controlled through external fields could potentially perform feats like precise remote surgery, targeted drug delivery, and fine mechanical work. One such rolling microbot design uses commercially available colloidal superparamagnetic beads which assemble in situ under an external rotating magnetic field into disk shaped "microwheels". This thesis further develops a technology that could have broad biomedical implications for enhancing modern drug delivery technology in challenging microenvironments.

First, we show that microwheels can travel up extreme inclines (80°), demonstrating that only a small load force is required to sustain rolling. At high concentrations, microwheels exhibit swarming modes which can be modified with specific magnetic field patterns. These modes enable unique functionality like fast velocity, high climbing rates, broad deposition, and local mechanical action to aid in drug delivery.

Second, we show that individual microwheel building blocks can be aerosolized into droplets which can travel through the air and then reassemble after landing on another surface. These reassembled microwheel swarms can enhance delivery by driving deeper into 3D printed lung models or can be specifically directed to target a chosen pulmonary branch.

Third, by using both magnetic force and torque, we show that microwheels can move on all surfaces regardless of their orientation. Since microwheels roll with simple rotating fields and very little load force, the required fields can be generated by a single rotating permanent magnet with three degrees of freedom. This simple technique enables swarm targeting in complex 3D capillary network models.

Fourth, an original open source microbot tracking software package is detailed that allows high throughput analysis of microscopy video. With this, large datasets can be extracted easily from multivariable experimental arrays. Additionally, individual microbots can be studied in detail using the trajectory inspector tool.

Together, the work presented in this thesis is a substantial step towards understanding and using this transformative microbot technology in a clinical setting. These novel techniques enable microbot movement in the complex 3D microenvironments in the body, including the pulmonary, gastrointestinal, and vascular systems.

TABLE OF CONTENTS

LIST OF FIGURES

ACKNOWLEDGMENTS

Thank you to my parents, whose lifelong support and encouragement have enabled me to pursue my doctorate and scientific career.

To Olivia, my partner, I owe thanks not just for the shared adventures we have experienced so far, but also for those in our future. Your consistent magnanimity, partnership, and motivation has had an enormous positive impact in my life.

I'm thankful for my friends and colleagues, whose collaboration, friendship, and camaraderie have profoundly influenced my life and research career. I look forward to continuing the lifelong friendships we started here.

Lastly, thank you to my advisor, David Marr. Your respectful leadership style and scientific prowess has served as a constant source of inspiration. I couldn't have asked for a better advisor or mentor.

CHAPTER 1 INTRODUCTION

1.1 Motivation

The treatment of many diseases is challenging due to the difficulty of delivering drug directly to the infected site. In standard disease treatment, drug is administered systemically within some therapeutic window[1] and at concentrations which are limited by the harmful side effects that can occur. Systemic treatment is therefore a balance between achieving maximum therapeutic benefit and avoiding systemic toxicity[2]. By instead delivering appropriate drug concentrations with targeting, local therapies can greatly exceed systemic values. Colloidal materials, particles with sizes from 10 nm to 10 μm, may be useful in biomedical applications due to their small size and ability to transport and concentrate therapeutic drugs in the body[3]. With proper targeting, colloids offer the potential for more effective treatment of diseases such as small vessel stroke[4], cystic fibrosis[5], recalcitrant bacterial infections[6], and cancer[7].

Microbots are actively directed micro-scale materials which move by converting external energy like light, ultrasound, or magnetic fields into local movement[8]. With this capability, microbots are of particular interest for biomedical applications because they could be remotely driven to a target site, perform surgery, and add mechanical action to increase drug delivery. Due to this promising ability, microbots have acquired a large research attention for improving the future treatment of difficult diseases. However, there are a variety of problems that need to be solved before clinical use. This thesis focuses specifically on the delivery movement of rolling microbot swarms in increasingly complex 3D microenvironments, building upon previous work on 2D surfaces.

1.2 Movement in Laminar Flow Regimes

At the scale of microbots, objects move differently than what is typical in the everyday world. Most locomotion techniques we are familiar with rely on inertial effects, using reciprocal motion like the spinning of boat motor blades or the kicking of a swimmer's legs. These approaches rely on pushing fluid quickly in the opposite direction of motion; however, they are not feasible in microenvironments. Motions such as these are best described using the Reynolds number relating inertial forces to viscous forces:

$$\mathrm{Re} = \frac{\text{inertial forces}}{\text{viscous forces}} = \frac{a v \rho}{\eta} \tag{1.1}$$

where a is particle radius, v is the particle velocity, ρ is the fluid density, and η is the fluid viscosity. In the world of microbots, the length scales (~1 μm) and velocities (10-100 $\frac{\mu m}{s}$) are so small that viscous forces dominate. This means that if a microbot is pushed along with a force which is suddenly removed, it will not continue moving, as its velocity will decay over an extremely small time scale. A peek into this

world was provided by E.M. Purcell[9] who described low Reynolds number behavior with the “scallop theorem”. A scallop moves by opening its shell slowly and then quickly closing it to jet out water and propel itself. In a low Reynolds number environment this locomotion technique will not work as the speed of the movement does not matter. As a result, bacteria and micro-organisms instead use a flagellum for translation. For example, a corkscrew-like motion is often used by bacteria to propel themselves through viscous fluids working like a wine corkscrew through cork. With each turn, the end “carves” its way forward. An alternative approach mimics neutrophils, which roll along walls, enabling locomotion by breaking flow-symmetry with a nearby boundary[10]. Independent of the propulsion technique, it is important to note that the microbot speed is proportional to its size. This results in a tradeoff where the maximum design size is limited by the target environment, but larger sizes are preferred due to increased speeds.

1.3 Microbot Design

For *in vivo* use, microbots must be constructed with biodegradable materials[11] or pretreated with biocompatible coatings. Common techniques involve sputtering microbots with titanium[12] or gold[13], or poly-ethylene-glycol (PEG) coatings[14]. Multiple methods exist for loading drug into microbots, including grid structures for stem-cell growth[12], compartments to hold drug particles[15], or utilizing surface chemistry to bind proteins[4]. While microbots can navigate using onboard fuel[14], [16] or by hijacking the body’s immune cells[7], [17], magnetic fields are particularly promising due to their existing use in medicine and ability to easily permeate through biological tissues[18]. Magnetic microbot design can vary widely but can be categorized based on their locomotion method.

Microbots that translate via a magnetic field gradient (magnetophoresis) including needles[19], rods[20], and capsules[21] typically require larger and more complex magnetic actuation systems as the magnetic field gradient has a fourth power decay with distance from the magnetic actuator. This results in limited clinical use due to the large coils and power supplies required to generate suitable precise fields for magnetophoresis. Earnshaw’s theorem also requires that a magnetic object must be monitored with constant feedback to hold its location in free space with magnetism if another constraining force is not present. Therefore, these microbots are most appropriate for procedures with constant precise tracking, such as ocular surgery[19]. Microbot designs of primary interest for procedures deeper in the body or without constant visual tracking are those which can be translated via magnetic field rotation. By utilizing magnetically applied torque, these microbots require weaker and less precise fields and include swimmers, which utilize the surrounding viscous fluid to “swim”, and rollers, which utilize nearby surfaces to translate.

1.3.1 Swimmers

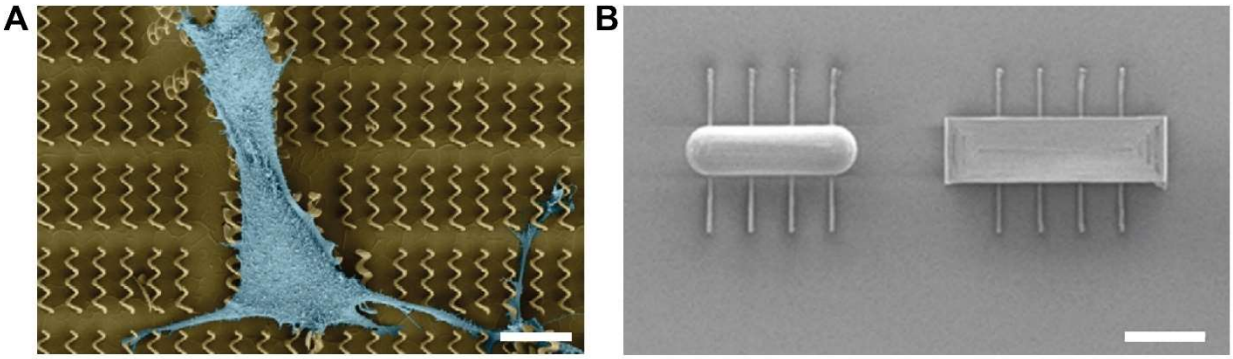

Figure 1.1 Swimming microbots. A) As-fabricated helical swimming microbots with a mouse myoblast cell[1]. Scale = 9 μm[22]. B) Cillary microbots that mimick microorganisms like paramecia[2]. Scale = 100 μm[23].

Swimmers utilize the surrounding viscous fluid to move by twisting either helical/corkscrew shapes or by non-reciprocal whipping of flagella. Some of these flagella require flexibility[24], [25] and are difficult to fabricate due to multi-material and multi-part designs making them impractical for mass application. Other designs rely on non-reciprocal actuation but suffer from low speed compared to their helical counterparts[23]. Helical swimmers, comparatively, can be fabricated in large numbers with precise and easily modifiable designs using direct laser writing (DLW)[11], [12] that can be tuned to their specific application.

While swimmers do not require a nearby surface to move, designing swimmers is a challenge that requires balancing sufficient size to allow appreciable speeds for macro-scale translation while still permitting penetration through pores or unobstructed flow through capillaries. For example, to penetrate through vitreous pores in the eye, small (~500 nm diameter) helices are needed[26]. While large helices (35 μm long, 8 μm diameter) can achieve speeds up to 180 μm s-1 at 1 mT, small helices (8.8 μm length, 2 μm diameter) can only achieve 30 μm s^{-1} at 4 mT[27]. 500 nm diameter helices used for drug delivery in the eye can achieve 10 μm s^{-1} through eye vitreous which, for movement from the cornea to retina, would take 40 min. We note that swimmers can be coated with substances like perfluorocarbon liquid to decrease the drag between the fluid and the swimmer, allowing for increased rotation rate at a given field strength in extremely viscous environments[26].

---

[1] Used under the CC BY-NC-ND 3.0 license from F. Qiu et al., "Bio-inspired microrobots," Materials Today, vol. 15, no. 10, p. 463, Oct. 2012, doi: 10.1016/S1369-7021(12)70201-8.
[2] Used under the CC 4.0 license from S. Kim, S. Lee, J. Lee, B. J. Nelson, L. Zhang, and H. Choi, "Fabrication and Manipulation of Ciliary Microrobots with Non-reciprocal Magnetic Actuation," Sci Rep, vol. 6, no. 1, Art. no. 1, Jul. 2016, doi: 10.1038/srep30713.

While helical microbots present a promising design for locomotion in open environments, the relatively large lengths (10-20 μm) needed to achieve appreciable speeds inhibit their application in circulatory environments. Also, when in high concentration, these helical microbots aggregate, decreasing their velocity[28]. Rolling microbot designs, however, can exhibit advantageous swarming behaviors at high concentrations that can increase velocity, penetration, or move cargo.

1.3.2 Rollers

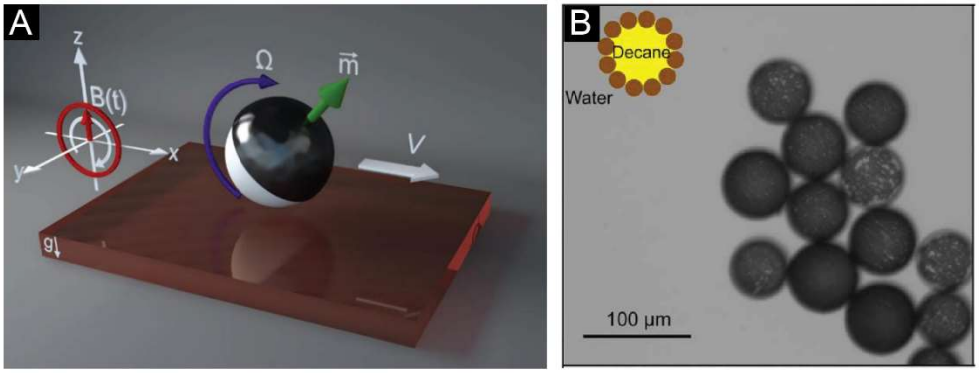

Figure 1.2 Rolling microbots. A) A ferromagnetic Janus microroller[3] rolls with velocity V when rotated with angular velocity Ω by the external magnetic field $B(t)$ [29]**.** B) Soft rolling pickering emulsion droplets[4] formed from decane and paramagnetic polystyrene beads[30].

Rolling microbots utilize nearby surfaces to break symmetry. Research suggests that for the majority of rolling microbots, there exists a thin layer of fluid between the microbot and the surface[31] and wet or static friction with a slipping coefficient[32]. Rollers can have many shapes and sizes, including peanut-shaped[33], diatomite frustules[34], Janus microsphere dimers[35], simple spheres[12], [32], soft pickering emulsion droplets[30], or colloidal spherical assemblies[36]. Previous research on colloidal microwheels has involved translation mechanisms[36], rolling on custom "microroads"[37], and drug delivery for fibrinolysis[4].

When large quantities of rollers interact with one another, macro-scale swarming behaviors arise with varying rotational fields. For ferromagnetic beads these behaviors include: vortexing, optimal for moving large cargo; tank-treading, for passing through narrow channels; and ribbons, for large-area small cargo movement.[33] Superparamagnetic beads at high concentrations can form μwheel agglomerations

---

[3] Used under the Creative Commons Attribution 4.0 International License: U. Bozuyuk, A. Aghakhani, Y. Alapan, M. Yunusa, P. Wrede, and M. Sitti, "Reduced rotational flows enable the translation of surface-rolling microrobots in confined spaces," Nat Commun, vol. 13, no. 1, p. 6289, Oct. 2022, doi: 10.1038/s41467-022-34023-z.

[4] Used under the Creative Commons Attribution 4.0 International License: Y. Gao, B. Sprinkle, E. Springer, D. W. M. Marr, and N. Wu, "Rolling of soft microbots with tunable traction," Sci. Adv., vol. 9, no. 16, p. eadg0919, Apr. 2023, doi: 10.1126/sciadv.adg0919.

hundreds of microns across at low frequencies, optimal for high velocities due to the increased circumference. Smaller wheel sizes can be selected by modulating the field rotation axis throughout a single rotation, resulting in a corkscrew like motion and increasing penetration[4].

Unlike swimmers, rollers require a force to provide sustained contact with a surface. To date studies have used the gravitational force due to high colloid density. To allow for translation on inclined, vertical, or inverted surfaces, other forces have been investigated. Acoustic forces can cause particles to gather close to a wall and, when combined with magnetic fields, can enable translation on vertical surfaces[10]. However, the acoustic force exerted on polystyrene particles is directly dependent on particle size and density and the fastest velocity for rolling microbots with an acoustic load force is 25 μm s^{-1}. Higher acoustic forces are not practical due to the formation of microbubbles in the bloodstream when strong fields are applied[38]. Use of acoustic fields *in vivo* are also limited by limited transmission through hard objects like bone[39].

By simultaneously applying a rotational field with a magnetic field gradient normal to a surface, rolling microbot speeds can be increased. With an additional load force of 0.2 F_g, it has been demonstrated that the translational velocity of a sphere can be increased from 40 to 80 μm/s with the same rotational field strength and frequency. This approach opens the possibility of translation of rollers on surfaces independent of a gravitational force[31].

1.4 Magnetic Actuation of Microbots

1.4.1 Theory

Maxwell's equations provide the foundation for study of magnetic fields; however, they can be simplified for normal descriptions of microbot behavior[40]. The magnetic field generated by a point dipole is commonly represented as

$$\mathbf{B}(r) = \frac{\mu_0}{4\pi}\left[\frac{3(\mathbf{m_m}\cdot\mathbf{r})\mathbf{r}}{r^5} - \frac{\mathbf{m_m}}{r^3}\right] \tag{1.2}$$

where **B** is the magnetic flux density vector or magnetic field strength, μ_0 the magnetic permeability of free space, **r** the distance, r the norm of **r**, and **m** the magnetic moment. The magnetic dipole can be generated by any magnetic material, including an electromagnet or permanent magnet. When analyzing the behavior of a microbot in a magnetic field, the effects can be split into force and torque components. The force, **F**, exerted on **m** is due to the spatial derivatives of the field, also known as the magnetic field gradient:

$$\mathbf{F} = \nabla(\mathbf{B}\cdot\mathbf{m}) \tag{1.3}$$

This force can pull microbots through a fluid, a process known as magnetophoresis. The torque exerted on $\mathbf{m}$ seeks to align the microbot dipole with the field direction and can be expressed as

$$\boldsymbol{\tau} = \mathbf{m} \times \mathbf{B} \tag{1.4}$$

This effect is often utilized with microbots to twist a helix[26], [27], [41], [42], roll a sphere[12], [32], [34], [43], or rotate a needle-like appendage[19], [44]. It is important to emphasize here that the magnetophoretic force is proportional to the magnetic field gradient while the torque is proportional to the field strength.

1.4.2 Magnetic Actuators

The devices used to create a controlled magnetic field can vary widely but generally consist of a series of wire coils or a collection of permanent magnets. Magnetic systems for targeted drug delivery have been heavily studied, analyzed, and iterated upon, especially within the last 10 years[45]. For microbots that navigate using magnetophoresis, full force and heading control is needed to point and move. This requires eight independent magnetic sources to control five degrees of freedom (DOF) in movement[46]. The sixth DOF, torque about the magnetization axis, is difficult to achieve due to $\boldsymbol{\tau}$ being orthogonal to both $\boldsymbol{m}$ and $\boldsymbol{B}$ (Eq. 3) which can only be achieved with a microbot with non-uniform magnetization[47]. One of the first devices capable of accurate control of these microbots is a hemispherical arrangement of eight electromagnets, termed OctoMag[19]. Variants of this hemispherical design have included optimization for smaller working volumes[48] and increased access[49], however, a hemispherical design is not required and other geometries such as planar[50] and cubic[51] have been investigated. Another design, termed an OmniMagnet[52], allows for movement of magnetic actuation devices around the working volume while still creating a field capable of 5-DOF. This design is optimized to use the dipole-field equation (1.2), simplifying the calibration and modeling needed to project a known magnetic field.

Microbots that utilize rotation to move require a much simpler magnetic actuation apparatus and can be used with low field strengths (1-20 mT). Traditional coil designs such as Helmholtz coils are designed to create a zero magnetic field gradient within their working volume. These coil systems are simple to construct, do not require detailed calibration of the working volume, and are typically used in studies of rotationally driven microbots[31], [33], [36], [37]. If a small gradient can be tolerated, approximate Helmholtz coils may be used, where the coils are arranged in a cube[45]. The individual coil design has also been shown to be non-critical, as an optimized tapered coil design results in only a 1.2% improvement over non-optimal cylindrical designs[53]. We also note here that an axial uniform gradient can be produced with a Maxwell coil arrangement, but often cannot be used simultaneously with weaker rotational fields due to competing magnetic torques on the microbot[45].

Permanent magnet designs present a simple method to project a known magnetic field. Many permanent magnet shapes can be used; however, for magnets shapes other than spherical, a multipole expansion of Eq. 3 is required close to the magnet[40]. Unlike electromagnet systems where the field is modulated using time varying currents, permanent magnet systems modulate the field by spinning and moving the magnet. Industrial 6-DOF robotic manipulators can be utilized to accurately move a magnet around the working volume while spinning at a known RPM[54], [55]. These permanent magnet actuation apparatus require less surrounding infrastructure to use, are generally cheaper, and can produce very strong fields (1.5 T) with a single magnet[45]. However, it is much harder to control the specific field design such as the ratio between the field gradient and strength. Also, in the case of equipment failure, a permanent magnet would need to be heavily shielded or moved away from the working volume to remove the magnetic field.

1.5 Biomimetic Models

While the ultimate goal is to test within biological models such as zebrafish larvae, mice, and eventually humans, simplified models are initially needed. It is difficult to fabricate realistic 3D biological models with established photolithography based microfluidic techniques. As an alternative, 3D printing technology presents an effective method to fabricate realistic models from high resolution scans of biological systems. Fabricating experimental models directly from 3D printing also benefits from faster production, easier iteration, and cost-effectiveness. However, due to the layer-by-layer nature of 3D printing, certain geometries are impossible to print without sacrificial support structures, presenting a challenge when printing negative biological models as channels must be strategically oriented to avoid blockages. Researchers have attempted to circumvent this disadvantage by instead printing sacrificial molds for PDMS casting[56].

Fused-deposition modeling (FDM) 3D printing is a much lower cost method but suffers from decreased resolution capabilities and increased print defects when compared to SLA 3D printing. However, it is important to note that models can be printed from common acrylonitrile butadiene styrene (ABS) plastic and can be used as a sacrificial mold for PDMS casting[57]. As ABS is soluble in acetone while PDMS simply swells, this method can be used to create complex geometries within PDMS if the print resolution is high enough. Multi-material FDM 3D printing can be utilized to print dissolvable support structures from poly vinyl alcohol (PVA), overcoming the aforementioned natural limitation of 3D printing. Additionally, 3D printing technology has improved vastly in recent years, resulting in higher resolution and cheaper printers capable of printing cells[58], hydrogels[59], [60], and flexible materials[61]. Overall, the 3D printing technology must be chosen according to the required characteristics of the model, such as high-resolution networks, surface properties, or cost.

CHAPTER 2 MULTIMODAL MICROWHEEL SWARMS FOR TARGETING IN THREE-DIMENSIONAL NETWORKS

Modified from a paper published in Scientific Reports[5]

C.J. Zimmermann[6], Paco S. Herson[7], K.B. Neeves[8,9], D.W.M. Marr[1,10]

2.1 Abstract

Microscale bots intended for targeted drug delivery must move through three-dimensional (3D) environments that include bifurcations, inclined surfaces, and curvature. In previous studies, we have shown that magnetically actuated colloidal microwheels (μwheels) reversibly assembled from superparamagnetic beads can translate rapidly and be readily directed. Here we show that, at high concentrations, μwheels assemble into swarms that, depending on applied magnetic field actuation patterns, can be designed to transport cargo, climb steep inclines, spread over large areas, or provide mechanical action. We test the ability of these multimodal swarms to navigate through complex, inclined microenvironments by characterizing the translation and dispersion of individual μwheels and swarms of μwheels on steeply inclined and flat surfaces. Swarms are then studied within branching 3D vascular models with multiple turns where good targeting efficiencies are achieved over centimeter length scales. With this approach, we present a readily reconfigurable swarm platform capable of navigating through 3D microenvironments.

2.2 Introduction

Actively manipulated microbots present a promising platform for targeted delivery of therapeutic drugs[8], [62] by swimming through bulk fluid[24], [27], [63], [64] or by utilizing nearby surfaces to roll[34], [36], [37], [65] or walk[66]. Using applied magnetic fields, individual microbots, proposed for applications including microsurgery[67], biofilm eradication[68], blood clot removal[4], and stem cell transplantation[12] with structures incorporating helical[44] or flexible components[25], can travel against fluid flow[69], [70] or at speeds up to 600 μm/s[71] in quiescent fluid. Though individual microbot translation can be accurately modeled[72], applications involving therapeutic payloads will require

---

 Sci Rep, vol. 12, no. 1, p. 5078, Dec. 2022, doi: 10.1038/s41598-022-09177-x.

[6] Department of Chemical and Biological Engineering, Colorado School of Mines
[7] Department of Anesthesiology, University of Colorado Denver | Anschutz Medical Campus
[8] Department of Bioengineering, University of Colorado Denver | Anschutz Medical Campus
[9] Department of Pediatrics, University of Colorado Denver | Anschutz Medical Campus
[10] Corresponding author

significant microbot numbers and concentrations where swarming behaviors, such as those demonstrated in nature with insects, birds, and fish, have been observed. Such emergent structures include vortices[33], [73], [74], ribbons[75], carpets[76], chains[77], or dispersions[78] composed of many individual microbots. In addition, swarms can be tuned to change modes to increase hyperthermia[79], travel in confined spaces[33], or increase translation in various bio-fluids[80].

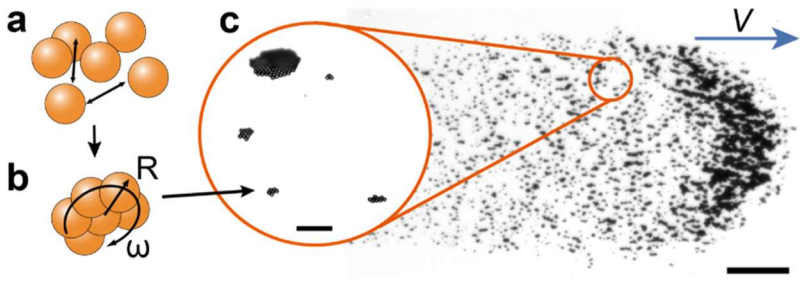

Figure 2.1 Upon application of a rotating magnetic field a) individual 4.5 µm beads form into b) µwheels which subsequently form into c) swarms. Inset scale = 50 µm. Swarm scale = 300 µm.

While precise microstructures can be fabricated[81], [82] with good translational control[83], microbots can be difficult to manufacture in bulk in the numbers required for therapeutic applications. Our previous work has focused on wheel-like microstructures (µwheels) that are reversibly and readily assembled *in situ* from superparamagnetic beads using a weak rotating magnetic field (Fig 1). Before assembly, these individual particle building blocks are small enough to pass through the smallest capillaries in the body and, when assembled into µwheels, can translate at velocities over 200 µm/s[36] on surfaces normal to gravity. For *in vivo* drug delivery however, µwheels will move as swarms (Fig 1). Others have shown microbot swarms with multiple modes in 2D[33], [77], here the contribution is microbot swarm targeting in 3D. During treatment, µwheel swarms may traverse environments such as the circulatory, digestive, or urinary systems that are curved, not normal to gravity, and contain tortuous pathways. An effective platform must therefore be able to navigate highly-branching and inclined systems. To investigate these, we first characterize the behavior of component µwheels in 3D and develop strategies for swarm movement that enable faster translation, better climbing, wider spread, and mechanical action. Then, we investigate the targeting efficiency of µwheel swarms in a model 3D network inspired by the cerebrovasculature. Together, this work presents a complete approach for quickly assembling superparamagnetic beads *in situ* into concentrated yet highly efficient multimodal µwheel swarms that can adapt to their environment and target across centimeter length scales. With this, we present a microbot-based approach that is not limited to 2D environments and can effectively target within 3D vascular analogues.

2.3 Results

2.3.1 µWheel Translation

Essential for predicting movement in realistic geometries, we begin by describing the behavior of individual µwheels on inclined surfaces where, upon application of a rotating weak magnetic field (~4 mT), µwheels assemble from 4.5 µm Dynabeads® into spinning clusters. While other superparamagnetic beads could be used, these highly-monodisperse particles consist of iron oxide domains within a polystyrene matrix, a relatively biocompatible material available at sizes that can be readily phagocytosed upon µwheel disassembly[84], [85]. In addition, their surfaces can be easily functionalized to create drug delivery vehicles as previously demonstrated[4]. When oriented with a component normal to the surface, µwheels roll at velocities which depend not only on the µwheel rotation rate, but also on the size (Fig 2a) and the camber, or tilt, angle θ of the µwheel relative to the surface normal. For this study we hold θ constant, focusing on the size and incline dependence of µwheel velocity. Unlike macroscopic wheels which move by gripping a solid surface, µwheels roll on an intervening layer of fluid and use wet friction to move. Their translational velocity can be predicted by balancing translational fluid drag and wet friction with the surface[36]. However, for translation up inclined surfaces the normal force, the µwheel distance from the surface, and the resulting frictional force are all altered. Accounting for this variable gap width, we develop a model (Fig 2b and Methods) that is valid across a broad range of incline angles 0-80°, enabling µwheel translation predictions while targeting.

With rotating magnetic fields of magnitude H, the induced magnetic torque can be expressed as[86] $\tau = nv\mu_o\chi''H^2$ where n is the number of beads in the µwheel, n is the volume of an individual bead, μ_o is the permittivity of free space, and χ'' is the imaginary part of the magnetic susceptibility. By approximating the viscous rotational µwheel torque with that of a disk[87] $\tau = 32\eta\omega R^3/3$ and equating torques, one expects a µwheel rotational frequency of $\omega = 3nv\mu_o\chi''H^2/32\eta R^3$. With a µwheel radius $R \sim n^{1/2}$ and for constant magnetic field strength we expect $\omega \sim 1/R$, a behavior we observe at all incline angles (Fig 2a), suggesting that the rotational drag dominates over drag from the surface.

As expected, small µwheels with R < 10 µm are less affected by a change in incline due to their lower weight (Fig 2b). However, large µwheels (> 35 µm radius), despite having significantly greater velocities on flat surfaces, are hindered by their mass and decrease in velocity. As a result and as the incline angle increases to 80°, µwheels greater than 35 µm in radius begin to slip backwards downhill as they roll (Supplementary Video 1). We also note that small µwheels (~10 µm radius) show only a 50% decrease in velocity at an 80° incline angle compared to 130% with large wheels (~60 µm radius), suggesting that only a small load force (< 1 pN) is sufficient to retain proximity to the surface and translate up steep slopes.

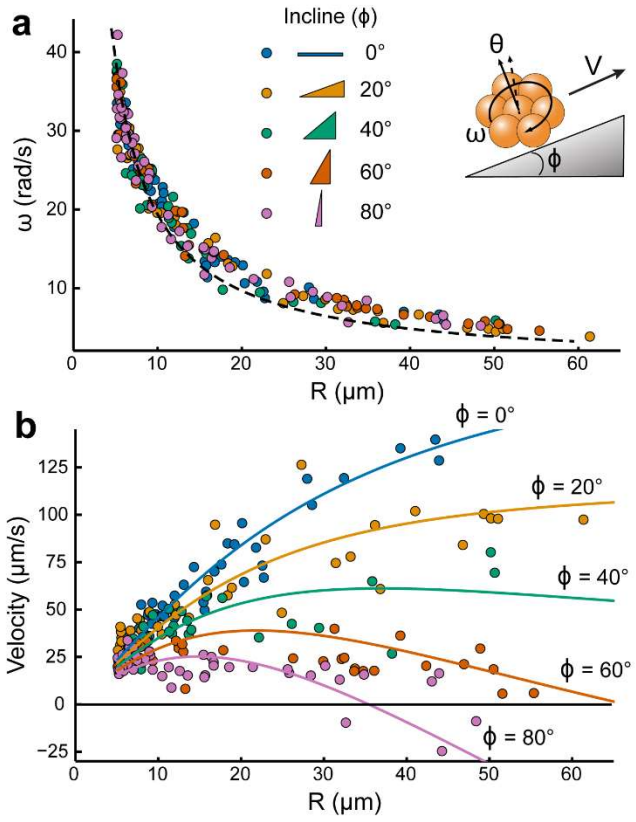

Figure 2.2 μWheel translation on inclines. a) μWheel angular velocity (ω) as a function of size (R) and incline angle (ϕ). Dotted line shows the $\omega \propto 1/R$ scaling. (inset) Translating μwheel on an incline. b) μWheel velocity over incline angles 0-80° with solid lines the variable gap width model (Supplementary Equation 1). All μwheels propelled with a constant 40 Hz circular rotating field of magnitude 3.7 mT and 30° camber angle, θ.

2.3.2 μWheel Swarming

For applications requiring therapeutic payloads for example, large numbers of μwheels will exhibit collective swarming behavior or modes which can be switched depending on the field and the subsequent component μwheel motion. At these high concentrations, μwheels collide and combine to form larger μwheels; however, we observe steady-state μwheel size distributions where growth plateaus. For example, for a 3.7 mT rotating magnetic field, the maximum observed wheel size is $R \sim 60$ μm. To understand this, we employ the Mason number[88], relating viscous to magnetic forces, Mn = Pe/λ with Pe the Peclet number, relating convection to diffusion, and λ the dimensionless dipole strength[89] given by $\lambda = \pi\mu_0 a^3 \chi^2 H^2/9kT$. By considering an individual bead at a μwheel edge we have $\mathrm{Pe} = 6\pi\eta a^3\dot{\gamma}/kT$ and $\mathrm{Mn} = 54\eta\dot{\gamma}/\mu_0\chi^2 H^2$ with $\dot{\gamma}$ the shear rate. With $\mathrm{Mn} \sim \dot{\gamma}$, small $\dot{\gamma}$ lead to small Mn where magnetic interactions create μwheel stability; however, as $\dot{\gamma}$ and Mn increase, viscous forces dominate, providing a significant energetic barrier to uncontrolled agglomeration in high shear environments. Probing further in the context of a rotating μwheel, we approximate the shear rate $\dot{\gamma}$ at the

outer edge with $\omega R/l$ where l is a characteristic fluid velocity decay length to obtain Mn = $54\eta\omega R/l\mu_0\chi^2H^2$ or Mn ~ ωR. Now recognizing from Fig 2a that, for constant fluid and field conditions, $\omega \sim 1/R$ and little variation in Mn with µwheel size is expected in our experiments. As a result, and due primarily to this slowing rotation with larger µwheels, we would expect continued growth if sufficient beads are available without changes in the applied field.

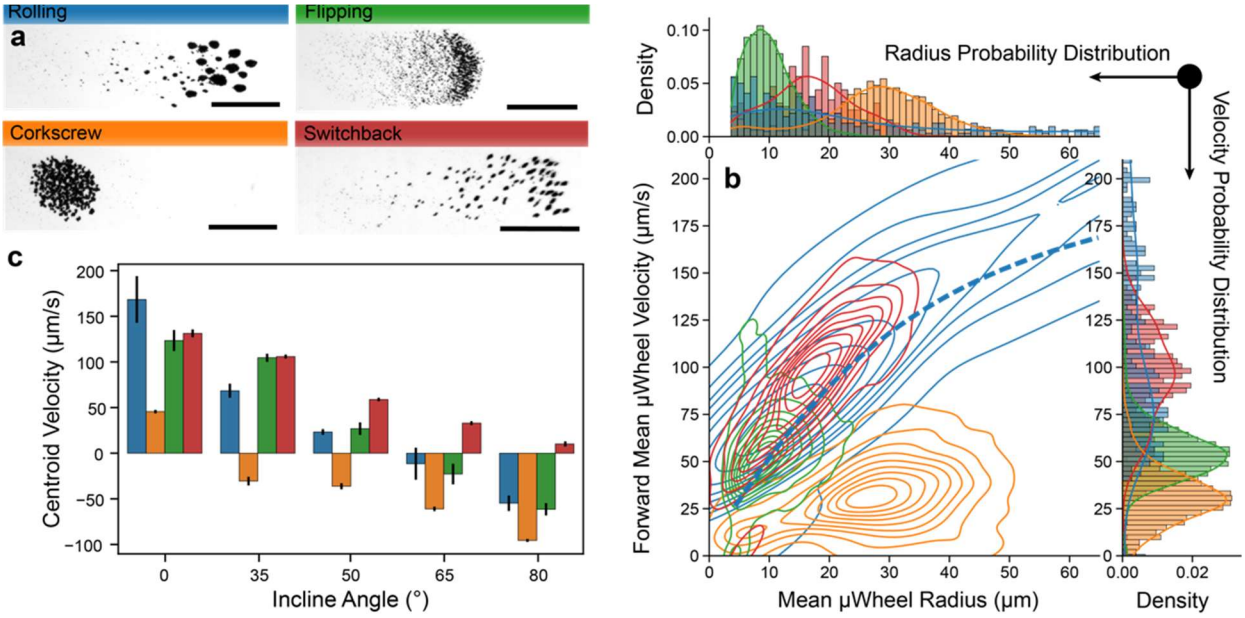

Figure 2.3 µWheel swarm characterization. a) Optical microscopy of four swarm modes after ~15 s of magnetic actuation. Scale = 1 mm. b) "Fingerprint" of each swarm mode. Blue dashed line is the model line at 0° from Fig 2b. Each probability distribution is fit with a kernel density estimate to guide the eye. c) Centroid, or center of mass, velocity of swarms at 0° and multiple steep angles. Error bars represent standard deviation of triplicate videos.

An effective approach for introducing shear and disrupting µwheel growth is with sudden changes in the heading direction or camber angle of the rotating field, where µwheels can separate into smaller components. Using different patterns of heading directions and camber angles (Supplementary Figure 1) and without varying the field strength or frequency, µwheel size distributions can be created and specific swarm modes specializing in various tasks designed. Here, we report four unique µwheel swarm modes which correspond to specific needs when targeting (Fig 3a): rolling mode, for optimal mass flux with quickly moving µwheels; switchback mode, for steep incline traversal using rapid turns; flipping mode, for deposition of small µwheels across a large area where µwheels are forcibly broken apart; and corkscrew mode, to support mechanical action by translating forward with a helical motion for enhanced penetration[4] (Supplementary Video 2).

Rolling mode is the simplest and results when the applied field is unchanged with the heading and camber angles kept constant (Supplementary Figure 1). Specializing in high mass transport, rolling mode

forms the largest μwheels that can quickly move across macroscale distances. As expected, it has the highest centroid velocity of studied swarms due to large μwheels; however, due to the lack of control on the μwheel size, a large range is formed, resulting in a significant spread. Flipping mode imparts rapid changes in camber angle which break up large μwheels resulting in small component μwheels. These smaller μwheels fall behind a concentrated front that breaks up with every change in camber angle, resulting in a deposition effect where beads are spread out over larger areas. Corkscrew mode, which has shown superior penetration into fibrin gels[4], uses a helical motion and gradually changing camber angles. This swarm sacrifices translation speed but retains a mid-range size distribution. The changing heading and camber angle (Supplementary Figure 1) enables this swarm to find the path of least resistance and avoid the formation of the largest μwheels. The helical motion due to the change in heading angle results in the slowest swarm mode. Switchback mode retains a constant camber angle but rapidly changes the heading direction, resulting in medium sized μwheels which perform better on inclines.

We track μwheel swarm movement at both the constituent μwheel (Fig 3b) and bulk (Fig 3c) levels and note that, for all swarm modes, the magnitude and frequency of the rotating magnetic field is kept constant. Using particle tracking, we obtain a unique "fingerprint" (Fig 3b) that describes the influence of field actuation on the component μwheel radii and velocity. For example, flipping mode selects small μwheels from 4.5 – 20 μm radius while rolling has a much broader size distribution. Likewise, the velocity probability distributions show that the back-and-forth helical motion of the corkscrew mode exhibits the lowest forward velocity. In general, the velocity and radius distributions are related; the larger the component μwheels, the faster the swarm translates. For comparison, we include the data of Fig 1b for individual μwheels along with the rolling swarm (Fig 2b, dotted blue line) where the swarm-induced broadening of the velocity distribution is apparent, suggesting that, while presumably weak, μwheel-μwheel interactions are having a significant impact on overall behavior.

To determine swarm mode climbing ability, we measure swarm bulk velocity up steep inclines (Fig 3c). In this, gravity slows swarm movement as angle increases with the switchback mode the only one able to translate up nearly vertical inclines. Such an alternating heading direction lowers the effective incline angle where the switchback angle φ, here 35°, results in a lower effective climbing angle $\phi_{eff} = \sin^{-1}(\sin(\phi)\cos(\varphi))$. For example, at $\phi = 80°$ choosing a switchback angle of $\varphi = 35^{\circ}$ results in $\phi_{\text{eff}} \approx 54°$. This technique is advantageous as it allows surface-enabled μwheel swarms to continue to move effectively up very steep angles without the use of additional external fields or magnetic field gradients. As ϕ increases, effective load decreases and μwheels, which require a load force normal to the surface and wet friction to translate, can no longer break symmetry and translate and simply sink due to their high density (Supplementary Video 3).

2.3.3 Targeting µwheel swarms in a three-dimensional network.

An effective drug delivery system requires sufficient microbot mass to reach the target area to provide a therapeutic drug dose. As all swarms are assembled and controlled using a global field, individual component control is not possible and variation in µwheel velocities causes a swarm mode dependent spread. Using tracking data from the swarm study (Fig 4a) and assuming a constant wheel distribution, a qualitative time-dependent mass distribution can be readily predicted (Fig 4b). Targeting with a global field requires the heading angle of the swarm to be changed when the most mass is near a target turn. While switchback mode exhibits decreased spread over long distances, rolling swarms provide the fastest mass transport of the swarm modes investigated here (Fig 3c). We therefore use rolling mode to quickly move mass over significant distances (~10 mm/min) for our study of payload targeting in macroscale 3D networks.

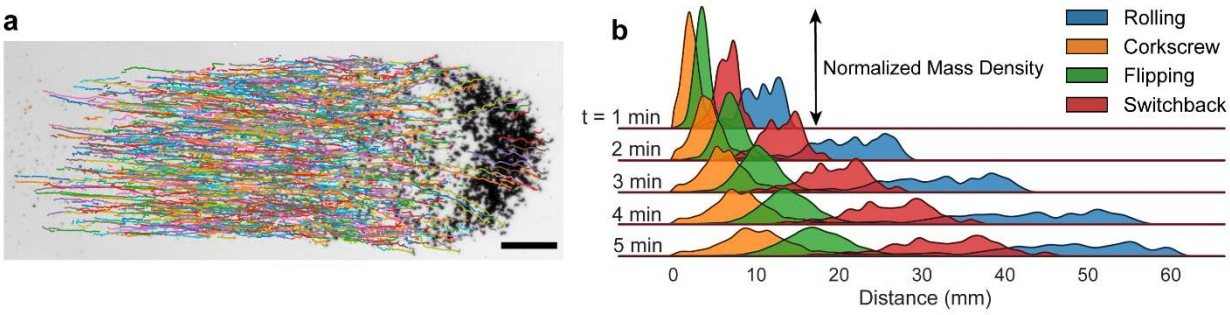

Figure 2.4 Spreading of µwheel swarms. a) Sample trajectory tracking in a flipping swarm after 20 s. Scale = 300 µm. b) Predicted mass transport of swarms based on measured velocity distributions. The shaded area under each curve is equal.

As a platform to test targeting, we fabricated clear 3D-printed branching models from an available murine cerebral model[90] and vascular atlas[91] of the murine middle cerebral artery (Fig 5a). In this device, we conducted 18 independent experiments targeting each of the six branches in triplicate to determine the µwheel swarm targeting efficiency, defined as the mass of beads in the target divided by the total mass injected (Fig 5d). For this study, the swarm was optically tracked and directed in real time. Using fluorescently-tagged µwheels, targeting efficiency can be directly observed after actuation (Fig 5c). From these experiments, we demonstrate that µwheel swarms can be translated over centimeters up and down inclined cylindrical channels with diameters ~0.6 mm and directed to a target vascular branch with efficiencies averaging ~38%. As expected, the targeting efficiency generally decreases as the distance from the start and the number of intermediary turns increases.

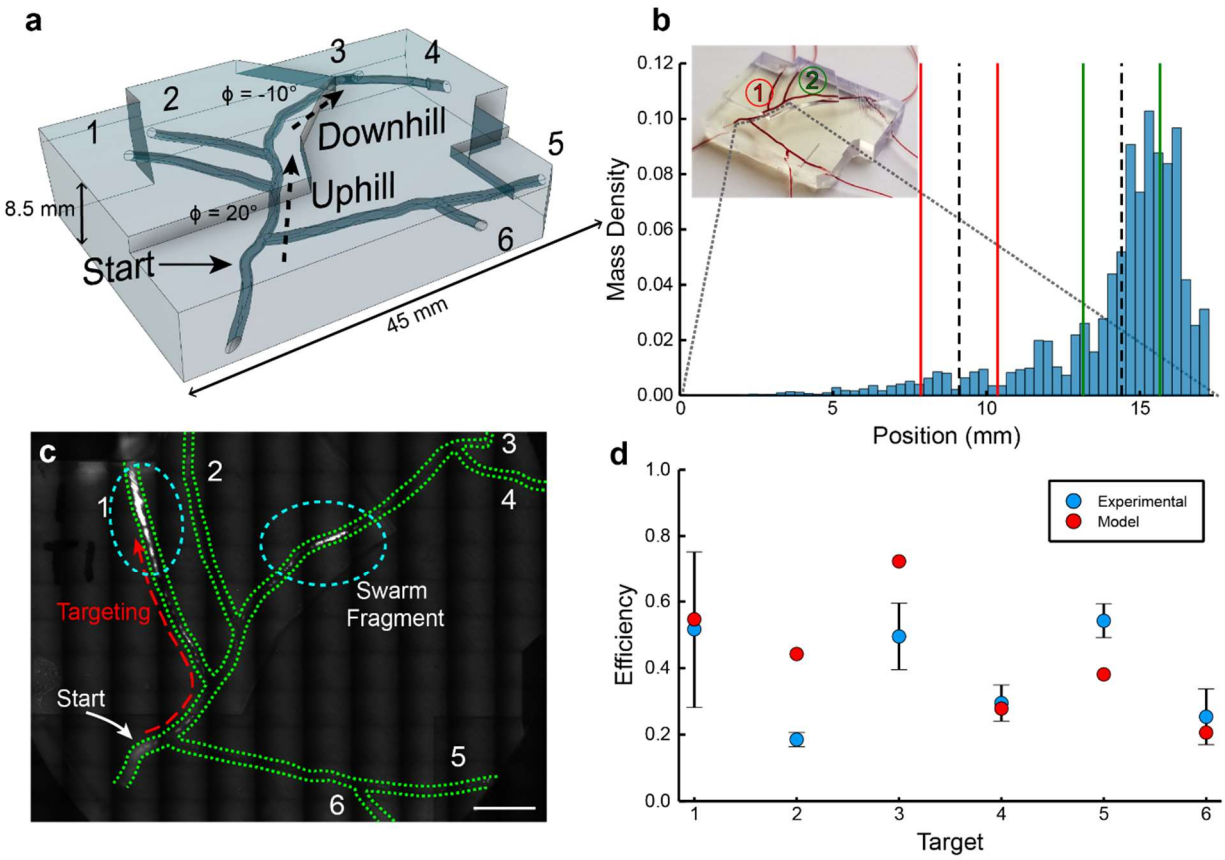

Figure 2.5 μWheel swarm targeting. a) CAD model of branching 3D vascular model. Each branch is labeled 1-6. b) μWheel bead density histogram of rolling swarm simulated ~14 mm into the device. Dotted lines signify the locations of the center of branches 1 and 2, while the bordering solid lines select which wheels are captured in each branch. c) Fluorescence scan after targeting μwheel swarm to branch 1. d) Experimental and modelled targeting efficiency of rolling μwheel swarm.

To predict targeting efficiency in a vascular mimic, we model μwheel swarm translation with an injection mass whose distribution evolves in time (Fig 4b). This allows a prediction of the evolution of the μwheel swarm at any point during targeting. In this simplified approach, we first use the previously measured component μwheel velocity and size distributions ($V(R, \phi)$, Fig 2a) to simulate the makeup of the swarm which can be integrated forward in time. Next, we recognize that a turn results in a fragment of the swarm tails being lost to untargeted branches (Fig 5b). Finally, the position of each μwheel x_i in the swarm is calculated through

$$x_i = \int_{t_{start}}^{t_{end}} V(R_i, \phi_i(x_i))dt \tag{2.1}$$

with ϕ_i the incline angle evaluated for each time step dt at the position x_i. This is achieved by encoding the 3D geometry of a network into a function $\phi_i(x_i)$. Despite the simplicity of the model, we

can predict targeting efficiencies within ~25% of the measured values (Fig 5d) using simple integration and histogram clipping, demonstrating the flexibility of this technique.

2.4 Discussion

We demonstrate here a potential drug delivery platform created from surface-enabled microbot swarms with switchable behavior, including targeting, penetration, climbing, and spreading. Swarms and the μwheels that comprise them are readily assembled in any desired quantity from commercially available superparamagnetic beads. Since the constituent beads do not attract without an applied external magnetic field, they reversibly disassemble into components small enough to pass throughout the circulatory system when the driving field is removed and transitions between swarm modes can be rapidly implemented. While surfactant was used here to decrease sticking, the beads could instead be functionalized with PEG[92] also increasing biocompatibility[93]. Our approach uses only weak magnetic fields for both assembly and movement and has been demonstrated here in low flow environments such as those associated with the vasculature near occluded channels[94]. We note that this approach is directly compatible with higher strength and other externally applied fields[31], [70]. Such a combination of fields may enable future swarm-scale targeting in flowing vascular networks, whole blood, or angles > 80° using an additional load force applied normal to the surface[31]. For flow, swarm modes with smaller component μwheel radii, such as the flipping or switchback swarms, would be best for sampling where fluid velocity is lowest.

Because μwheels are reversibly assembled from individual beads with application of a magnetic field, the effects of field switching are immediate (~10 ms) and achieved at the sub-μwheel level. As a result, μwheel swarms can readily switch modes, allowing adaptable travel through complex environments. Rolling mode with large μwheels could be used for quick translation until a steep incline is reached where switchback mode would be used. Flipping mode forms the smallest μwheels and could then be used to navigate in the most constrained spaces. After reaching the target site, flipping mode could be used to spread μwheels across a target patch (Supplemental Video 4) or corkscrew mode could be used to penetrate through a blockage. Our work to date has demonstrated the use of corkscrew mode on fibrin gels[4] where the helical turn and camber angle rotation frequencies could be readily tuned depending on the target blockage. Of significant note here is that all assembly, translation, and swarm movement for all modes do not require gradient magnetic fields which are difficult to scale to larger sizes but instead use a global weak field (~4 mT) that acts uniformly through the working volume.

While we observe that μwheel swarms have weak μwheel-μwheel interactions that lead to swarm dispersion, over macroscale distances they can still achieve good targeting efficiencies (Fig. 5d) which are not limited by swarm velocity, but rather by swarm dispersion and global control. While other researchers have successfully tuned paramagnetic swarming microbots for attractive interactions[77], they often

report low (< 10 μm/s) swarm velocities. Our approach emphasizes targeting speed as an important variable, especially important for treatment of diseases like stroke where timing is critical. If translation with lower spread is needed, other modes can provide a more cohesive swarm due to their lower μwheel size variance (Fig 4b).

We show that μwheels can translate up steep inclines and their behavior is captured with a variable gap width model. We calculated these gaps across a wide range of incline angle and μwheel radii (Supplementary Figure 2) by a simple balance of load and electrostatic repulsion and confirmed that gap width decreases up to 70% with increasing load force. Surprisingly, μwheels can travel up inclines as steep as 80˚, providing access through most geometries and showing that swimming microbots are not required to locomote in complex 3D networks. They do so by using switchback turns and selected optimal μwheel sizes to transport large quantities of beads up steep inclines, an actuation approach that greatly extends the 3D locomotion ability of surface-enabled microbot swarms.

Finally, we demonstrate that μwheel swarms can quickly and successfully target in 3D environments. By combining our individual μwheel model with swarm component radius distributions, we can predict whole swarm movement and targeting efficiency within ~25% through arbitrary 3D geometries. While we currently direct μwheel swarms manually via joystick for all presented experiments, future work could automate turn heading angle changes for autonomous control if real-time tracking is difficult in the target geometry. Additionally, high resolution scans of target systems in the body are routinely conducted for *a priori* knowledge of the targeting environment. Not only is this important to identify treatment location, but the exact layout can vary widely from person to person[95]. This emphasizes the value of techniques that can predict microbot distributions and targeting efficiencies in arbitrary targeting pathways with inclines and bifurcations. We focused here on rolling mode due to its superior mass transport and lack of steep inclines in the target model. Future work will focus on optimization strategies for switching between modes depending on the challenges of a particular target network.

2.5 Materials and Methods

2.5.1 Rotating microscope

Visualization of μwheel translation on non-horizontal surfaces requires an apparatus in which the incline angle can be changed while keeping the electromagnet and microscope arrangement fixed. To achieve this, a custom-built 3D printed microscope and actuation system was fabricated (Fig. 6) where coils supply the rotating magnetic fields in tandem with established signal generation software[96]. The z axis consists of two 50 mm i.d. 400 turn coils above and below the sample. The x and y axes have two pairs of coils each of which are comprised of a 50 mm i.d. 400 turn coil and 65 mm i.d. 400 turn outer coil. The optical train consists of a high-speed camera (Epix SV 643M), optical tube, and switchable objective (Olympus) attached to a three-axis micrometer for movement of the optical train along with a

dimmable LED light source (Luxeon 5000K, Alberta, Canada). The entire device is attached to a precision rotation stage (UTR120, Newport) to allow for specification of incline angle.

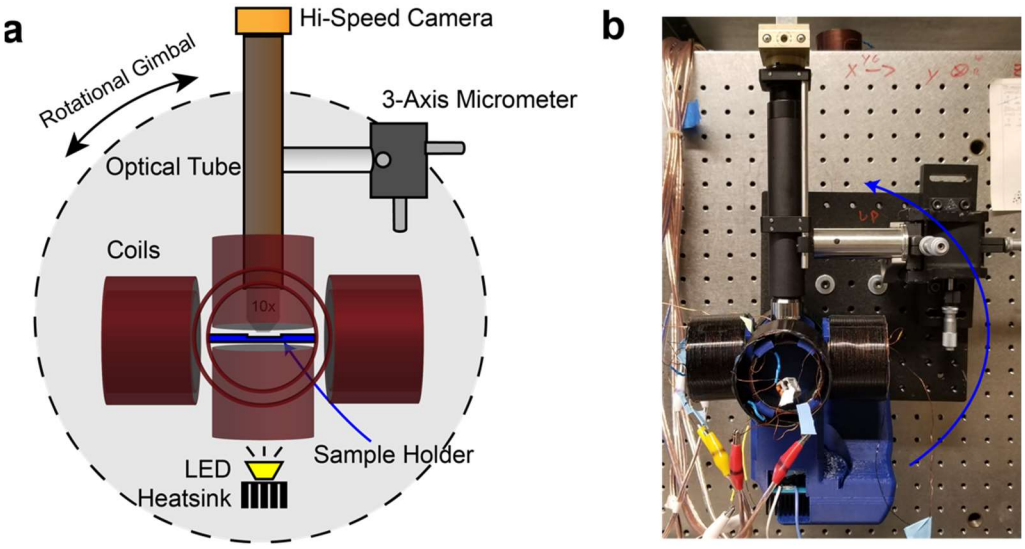

Figure 2.6 Rotating microscope and actuation apparatus. a) Diagram depicting the optical train the coils. 10 coils in total are depicted here, with 2 sets of concentric coils on the x and y axes and 2 individual coils on the z axis. b) Fabricated apparatus. The body is 3D-printed out of poly-lactic acid (PLA) polymer while the gimbal is mounted behind the black optical board.

2.5.2 Component µWheels on Inclines

The sample chamber consists of two square 22 mm glass cover slips of 0.17 mm thickness sandwiching a 0.5 cm ID gasket cut from double-sided tape (RP32 VHB™ tape, 3M, Maple, MN). This 800 µm tall gasket allows for large µwheels to travel unimpeded by the top surface. A 12 µL sample of 4.5 µm superparamagnetic beads (Dynabeads® M-450 Epoxy, Thermo Fisher) diluted 125x with 0.2 weight % sodium dodecyl sulfate (SDS) (Sigma-Aldrich) is used for all µwheel experiments to prevent aggregation between particles and surfaces. Additional 0.2% SDS solution was added to fill up each sample chamber before closing. A standard rotating magnetic field was used for all experiments with a field strength of 3.7 mT, 40 Hz, and 30° camber angle[96]. All µwheel tracking was performed using custom particle tracking software MuTracker with the complete source available on GitHub[97]–[100]. The rotation rate of most µwheels was calculated through the fast Fourier transform of the rotation angle of the fit ellipse. The highest peak of the frequency domain corresponds to one half of a µwheel rotation. This method fails for radially symmetric µwheels and, in this case, the rotation rate was determined manually.

We describe motion on inclines using a model where the μwheel weight, W, can be expressed as $W = mgn$ with N the normal force, m the mass of an individual bead, g the gravitational acceleration, and n the number of beads in a μwheel. Though previous work has considered a camber angle dependent load[36], here we omit because the camber angle used is small and held constant. For inclines in 3D, we split the weight into a normal y component, $W_y = mgn\cos(\phi)$, and a parallel x component, $W_x = mgn\sin(\phi)$, with ϕ the incline angle (Fig 2A inset). We have previously shown that the fluid gap, δ, between a μwheel and the surface is analogous to the hydrodynamic lubrication region that exists between two fluid-lubricated solids[31]. The load force varies widely due to R and ϕ suggesting an approach that considers a variable fluid gap width. To approximate this gap width for a wide range of μwheel radii (5 - 70μm) and incline angle (0-80°), we balance the forces in the normal y direction:

$$\sum F_y = W_y - F_{es} = 0 \tag{2.2}$$

with F_{es} the electrostatic force, approximated for an individual bead wall interaction by[65], [101]:

$$F_{es} = 4\pi\epsilon\epsilon_0 a\kappa\nu_1\nu_2 e^{-\kappa\delta} \tag{2.3}$$

with ϵ the permittivity of the medium, ϵ_0 the vacuum permittivity, a the radius of a bead, κ^{-1} the Debye length, and ν_1 and ν_2 the zeta potential of the particles and the near surface, respectively. However, because of asymmetry and spin, the actual distance between the wall and μwheel will not be that of a simple sphere. To account for this we include a fitting parameter k_1 and solve for the gap width to obtain:

$$\delta = k_1\kappa^{-1}\ln\left(\frac{4\pi\epsilon\epsilon_0 a\kappa\nu_1\nu_2}{mgn\cos(\phi)}\right) \tag{2.4}$$

With experimental data we find k_1 = 1.50, indicating the observed non-circularity of measured μwheels across the large range of radii. Calculated separation heights are in Supplementary Figure 2. We next balance the forces in the direction of propulsion x:

$$\sum F_x = F_f - F_d - W_x = 0 \tag{2.5}$$

with $F_f = \mu_k W_y$ the wet friction force and F_d the drag force. We approximate F_d using an analytical solution for viscous drag on a cylinder[102]

$$F_d = k_2\frac{8\pi a\eta V}{ln\left(\frac{2(R+\delta)}{R}\right) - \frac{1}{4}\left(\frac{R}{R+\delta}\right)^2} \tag{2.6}$$

along with another fitting parameter k_2 for irregular μwheel shape with η the dynamic viscosity and V the velocity of the μwheel. With experimental data we determine that $k_2 = 3.11$ suggesting that the increased surface area caused by a collection of spheres compared to a smooth cylinder systematically increases the drag force. To determine the wet friction coefficient μ_k, we balance the frictional torque, $T_f = \mu_k W_y \times R$, with the torque required to shear the lubrication fluid layer, $T_{shear} = \tau A \times R$, with A the contact area and the fluid shear stress τ, which by assuming a linear velocity profile can be expressed as[36]

$$\tau = \eta \frac{\partial V}{\partial y} \approx \eta \frac{\omega R - V}{\delta} \tag{2.7}$$

By then approximating the contact area of the μwheel $A \approx Ra$, one obtains

$$\mu_k = \frac{\eta a}{\delta W_z} R(\omega R - V) \tag{2.8}$$

with ω the angular velocity. Finally, using $n \approx \left(\frac{R}{a}\right)^2$ we arrive at a model that can predict the velocity of component μwheels across wide ranges of incline angles and radii (Eq. S1, Fig 2b). Supplementary equation 1 with fit parameters k_1 and k_2 is used to predict individual μwheel velocity during targeting in 3D models.

2.5.3 μWheel Swarms

An identical sample chamber, solution, and magnetic field (see μWheels on Inclines) was used for all swarm experiments, except for an increased bead solution of 15 μL. Before each video, a permanent magnet was used to collect beads on the top of the sample chamber before removing the magnet and letting the beads settle for ~10 s. Each swarm mode video was performed in triplicate across all incline angles presented here (see Rotating Microscope).

Particle tracking was performed using open source software MuTracker[100] which identifies and tracks the trajectories of all μwheels. The output of the software is the mean μwheel velocity and the mean radius of every μwheel in the swarm. However, in the event of a collision between two μwheels, one trajectory ends while the other's velocity and radius is increased to the mean before and after the collision. The reverse occurs during a splitting event.

2.5.4 3D Printed Mouse Middle Cerebral Artery Model.

We fabricate 3D microfluidic devices using a Form 3 stereolithography (SLA) 3D printer (Formlabs Inc, Somerville, MA). Using available models of the mouse brain from the Allen Reference Atlas[90] and a mouse cerebrovascular atlas[91], a tracing of the MCA was projected onto the curvature of the surface

of the brain using computer-aided design software (Fusion 360, Autodesk). A selection of the MCA was cropped and designed into an enclosed microfluidic device with seven outlets and multiple viewing windows. Each inlet was plumbed with 0.01" ID by 0.030" OD clear Tygon® tubing (Cole Parmer) and fixed in place with two-part epoxy. A new microfluidic device was printed for each experiment to avoid residual fluorescence from stuck particles at junctions.

2.5.5 Fluorescently labeled beads

To enable targeting efficiency quantification, 20 µL of 4.5 µm epoxy Dynabeads® were incubated in 0.1 mg/mL rhodamine B (Sigma Aldrich) for 24 hr. After incubation, the beads were washed five times with 0.2 wt % SDS solution. The bead solution was stored in darkness until used, and, if greater than 5 hr elapsed, were washed 3x using the same process to remove any desorbed rhodamine B.

2.5.6 Targeting in MCA Model

To demonstrate targeting, the fabricated MCA microfluidic devices were first loaded with 0.2 wt % SDS in deionized water. Fluorescently labeled beads were localized at a defined start area using a permanent magnet while 20 µL of fluorescently labeled bead solution was injected into the closest bottom inlet. All tubing was clamped, and the device placed on a fluorescence-capable microscope with a motorized stage (Olympus IX81). A full scan using a TRITC filter was performed before each experiment to determine the number of beads injected. The device was then placed for observation and targeting on a separate fluorescence microscope (Olympus OpenStand) fitted with five identical 50 mm i.d. 400 turn coils. These coils are similar to those used for the rotating microscope except they lack a sixth coil above the sample. Using a joystick to orient the 3.7 mT rotating field, the particles were assembled into a swarm and directed towards the targeted vascular branch for a maximum of 10 min. The device was then transferred back for a full scan to determine the percentage of beads in each region of interest (ROI).

2.5.7 Simulation of Swarms in Arbitrary Models

From the rolling swarm radius distribution (Fig 3b), the mass of each µwheel was estimated assuming hexagonally close packed beads and the distribution normalized by the total swarm mass. The geometry of the model was characterized with $\phi_i(x_i)$ using the position and incline angle at each junction. Using linear interpolation between junction points, the angle at any position in the network could be determined. For the case where a turn was followed by another turn, a separate incline function was defined for each branch. For each simulation, the swarm was initialized at the start position with each µwheel at $x = 0$ and then numerically integrated using Euler's method with a time step of 0.1 s and Supplemental Equation 1 using $\phi_i(x_i)$ at the µwheel current position. After each step, the mass weighted position mean of the entire swarm was used to identify the swarm centroid location. This process was continued until the

centroid position was greater than the desired turn location. μWheels that successfully continued targeting were those within 0.5σ of the turn point, where σ is the weighted standard deviation of the swarm. For the case where there was a parallel channel nearby, the μwheels within 0.5σ of the parallel channel were considered lost (Fig 5b). This procedure was continued until the swarm made all necessary turns to reach the target branch. To simulate collection in a target branch, the swarm was integrated forward until the mass weighted mean advanced 1 mm where all mass remaining was counted as successfully targeted.

2.5.8 Bead Quantification and Targeting Efficiency

For all fluorescent quantification, each 16-bit image was first thresholded to remove the background noise (pixels with intensity < 3600) thereby isolating the bead fluorescent signal. To determine the fluorescence per bead, a glass slide with fluorescently labeled beads was placed on the same microscope in which scans of the device were performed. A picture was taken with the same settings and light source intensity. The beads were then manually counted and divided by the total brightness signal in the image to calculate the number of beads per fluorescent count. For targeting experiments, ROI masks for each branch were created and exported using Fiji[99]. Using Python, the targeting efficiency was calculated by dividing the fluorescence intensity in the target ROI after targeting by the total fluorescence intensity before targeting.

2.6 Acknowledgments

The authors acknowledge support from the National Institutes of Health under grants R21AI138214 and R01NS102465.

CHAPTER 3 DELIVERY AND ACTUATION OF AEROSOLIZED MICROBOTS

Modified from a paper published in Nano Select[11]

Coy J. Zimmermann[12], Tyler Schraeder[12], Brandon Reynolds[12], Emily M. DeBoer[13], Keith B. Neeves[14], David W.M. Marr[12]

3.1 Abstract

For disease of the lung, the physical key to effective inhalation-based therapy is size; too large (10's of μm) and the particles or droplets do not remain suspended in air to reach deep within the lungs, too small (sub-μm) and they are simply exhaled without deposition. μBots within this ideal low-μm size range however are challenging to fabricate and would lead to devices that lack the speed and power necessary for performing work throughout the pulmonary network. To uncouple size from structure and function, here we demonstrate an approach where individual building blocks are aerosolized and subsequently assembled in situ into μbots capable of translation, drug delivery, and mechanical work deep within lung mimics. With this strategy, a variety of pulmonary diseases previously difficult to treat may now be receptive to μbot-based therapies.

3.2 Introduction

The promise of micro-scale devices capable of medical intervention has led to the development of microbots (μbots) that swim, crawl, and roll (1–4). With sizes ranging from the 10's to 1000 μm (5) and designed for movement and delivery through the blood stream or GI tract, potential applications range from disease diagnosis (6) to targeted therapies for stroke (7) and cancer (8). For diseases of the lung however, aerosolization provides a more direct route for delivery to the airway. Aerosol-based therapies have been used for centuries to treat asthma and persistent cough and, with the advent of metered dose inhalers in the 1950's, use has significantly increased (9). The efficiency and effectiveness of aerosolized treatment however is significantly reduced in diseases where fluid buildup creates transport barriers to underlying biofilms and epithelial cells (10, 11). Common examples include pneumonia, cystic fibrosis, acute bronchitis and chronic obstructive pulmonary disease. With their potential to enhance in vivo transport, μbots could be used to overcome fluid buildup and enhance treatment. Often fabricated using

---

 Nano Select, p. nano.202100353, Mar. 2022, doi: 10.1002/nano.202100353.

[12] Department of Chemical and Biological Engineering, Colorado School of Mines, Golden, CO 80401, United States

[13] Department of Pediatrics, University of Colorado Denver | Anschutz Medical Campus, Aurora, CO 80045

[14] Departments of Bioengineering and Pediatrics, Hemophilia and Thrombosis Center, University of Colorado Denver | Anschutz Medical Campus, Aurora, CO 80045, United States

techniques adapted from the microelectronics industry (12), µbots can be powered and directed by a variety of fields, including magnetic (13), acoustic (14), chemical (15), and even optical fields (16). For in vivo application, µbots are most commonly controlled via magnetic fields which do not attenuate in tissue (17) and have demonstrated directed translation via swimming (18, 19) and rolling (7, 20) for drug delivery (2, 21) within aqueous environments. Delivery through air for lung-based therapies however requires additional considerations that limit the use of most current µbot strategies. With physical principles similar to those for airborne transmission of disease (22), inhaled drugs must be formulated within a specified size range. The optimum aerodynamic size for drug-laden aerosols is in the range of 1-5 µm (23), commonly delivered via nebulizer to define a desired particle size distribution that determines the deposition profile within the lungs (24). Here, we aerosolize 4.5 µm building blocks via droplets that, once delivered into a liquid film within the lung, can subsequently assemble into larger µbots that can quickly translate at speeds up to 200 µm/s and perform work.

3.3 Results and Discussion

Viscosity plays a dominant role in locomotion at small length scales (25). Microorganisms overcome this through physical adaptations, like rotating flagellum, that are difficult to artificially replicate and control (26, 27). In a particularly non-biomimetic approach, we have demonstrated a rapid and reversible µbot fabrication and powering method where µm-scale superparamagnetic beads assemble into µwheels upon application of a rotating magnetic field (20). These µwheels roll rapidly and can be immediately redirected with a simple alteration in the magnetic field orientation resulting in speed and heading changes. Because the approach relies on the assembly and rotation of µbots in a weak magnetic field, it does not require high fields and strong field gradients necessary for magnetophoresis. We note that, because beads are available with a variety of surface functional groups, a variety of biological agents can be attached to the surface and the µwheels used as a drug delivery vehicle (7).

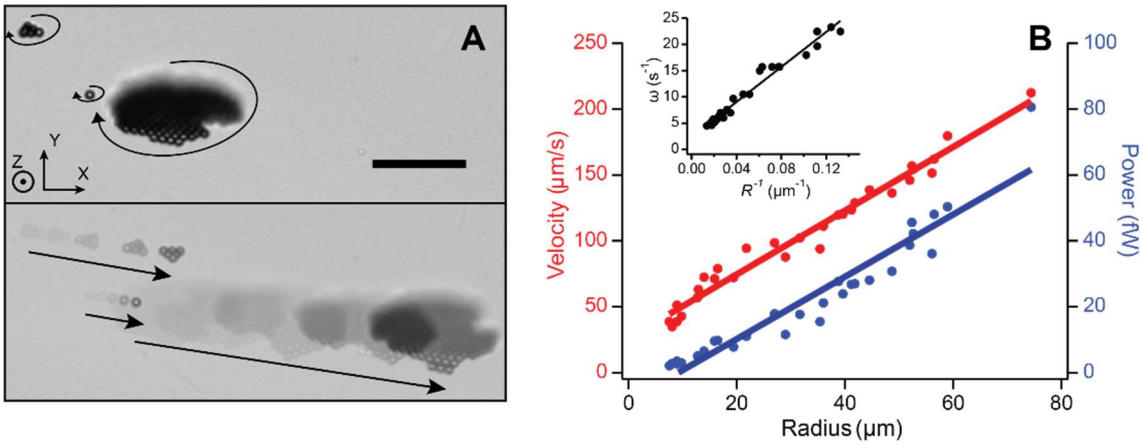

Figure 3.1 A) Wheel rotation and translation in 2 s with applied rotating magnetic field with axis of rotation $\hat{\boldsymbol{\Omega}} = \left[0, \cos\left(\frac{\pi}{6}\right), -1/2\right]$. 4.5 μm diameter beads, f = 40 Hz, magnetic flux density B = 3.4 mT, scale bar = 50 μm. Note larger μwheels translate faster than smaller ones (Supplementary Video 1). B) Velocity and power dependence on assembled μwheel size with linear fits to expected behaviors. Inset: μWheel rotation rate ω scales as 1/R.

In this approach upon application of a magnetic field, superparamagnetic beads experience strong attractive interactions, bringing them together to assemble into two-dimensional structures of varying shapes and sizes. With rotation of the magnetic field, these structures spin and, with orientation of the field axis off the surface normal, μwheels translate (Figure 1A). Under fixed applied field conditions we measure the radius R, the rotation rate ω, and the translational velocity V to determine the power P via the rotational torque required to spin the μwheel. With μwheels powered via rotating magnetic fields of magnitude H, the magnetic torque induced can be expressed (28) as

$$\tau = N v \mu_o \chi'' H^2 \tag{3.1}$$

where N is the number of beads in the μwheel, n the volume of an individual bead, μ_o the permittivity of free space, and χ'' the imaginary part of the magnetic susceptibility. By approximating the viscous rotational μwheel torque with that of a disk (29)

$$\tau = 32\eta\omega R^3/3 \tag{3.2}$$

with η the viscosity, one obtains

$$\omega = 3Nv\mu_o\chi'' H^2/32\eta R^3 \tag{3.3}$$

and, with a μwheel radius $R \sim N^{1/2}$, estimated from the two-dimensional planar disk area R^2 divided by the cross-sectional area of a single bead, we expect $\omega \sim 1/R$. Similarly, and with $P = \tau \cdot \omega$, we expect $P \sim \omega N \sim R$, a linear dependence on size, driving the need for larger μwheels that can perform more mechanical work or apply more power over a given amount of time. In addition to the available power,

μwheels move at a velocity $V \sim \omega \cdot N$ (20) leading to $V \sim R$ with larger μwheels translating faster (Figure 1B). Because both power and velocity are proportional to size, and while analogous nano-sized bots could be inhaled, they could not do significant work or be readily driven to desired sites once delivered. As opposed to approaches that use external fields to bias the impaction of inhaled nanoparticles (30, 31), airborne transport of μbot building blocks for subsequent assembly overcomes these issues. Here, and to deliver μwheels, we first seed aerosol droplets with individual 4.5 μm beads for delivery into lung mimic airways. After delivery inside the airway, μwheels assemble in the aqueous film formed from the aerosol and are free to translate deeper into the lung (Fig 2A). Assembly of μwheels in situ has significant advantage as the building blocks are small enough to be aerosolized and delivered into lung pathways. Of additional note is that particles > 6 μm size (32) are less susceptible to macrophage scavenging (33) once delivered, further motivating the use of larger μbots. Because assembly is reversible, upon removal of the magnetic field, μwheels disassemble into individual beads for elimination by these natural mechanisms for dust and other foreign particles in the mucus lining (34). Additionally, these beads have been shown to have similar histological scores to alginate, a bio-inert material commonly used in biomedical applications (35).

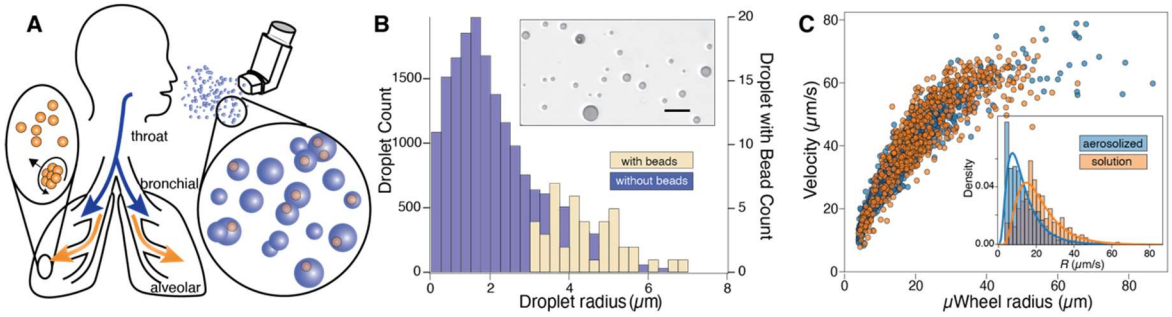

Figure 3.2 A) Concept illustration. B) Measured size distribution of aerosolized droplets with bead-containing drops identified. The overall fraction of droplets containing beads = 0.235%. Scale bar = 20 μm. C) Pre- and post- aerosolization μwheel sizes and velocities. f = 40 Hz, B = 2.1 mT. Note that both demonstrate similar behavior with size; however, a histogram of μwheel radii (inset) shows the μwheel distribution post aerosolization is shifted to smaller sizes.

To aerosolize the beads, a fluid aliquot containing beads is combined with an air stream inside a clinically and commercially available nebulizer, the flow rate of which determines droplet size distribution (24). We measure this distribution by directing aerosolized droplets into oil for subsequent imaging via optical microscopy (Figure 2B inset) where both droplet size and particle containing distributions are determined. Once aerosolized, we direct the droplets to surfaces where they impact, coalesce, and create a liquid film containing dispersed beads (Supplementary Video 2). The primary mechanisms of aerosol delivery are inertial impaction, gravitational sedimentation and Brownian

diffusion (36). With these, larger particles > 5 μm tend to embed in the upper airway while smaller < 0.1 μm particles have the highest likelihood of making it deep within the respiratory tract. Though most are simply exhaled, such smaller particles can reach the lower bronchioles and alveolar lung regions where particle size would need to be 10 nm to reach via diffusion (34, 37). While certainly aerosol-based drug delivery approaches use particle size in their targeting design, to do mechanical work or translate effectively once embedded, larger particles are required. Here the beads we use are available in the 1-5 μm range, overcoming the drawbacks of deposition in the upper airways by making available new mechanisms, including in situ assembly and rolling, to transport deeper into the lungs when desired.

As described previously and upon application of a weak rotating magnetic field, individual beads assemble into μwheels that use wet friction to move. To demonstrate that aerosolization does not negatively impact μwheel function, we compare velocities of μwheels composed of beads from solution to those assembled from aerosolized droplets (Figure 2C). In this, droplets are initially formed within an aerosolizer and condense on a surface in sufficient quantity to form a liquid layer. Within this layer and upon application of the magnetic field, beads assemble into μwheels with a velocity vs. size relationship (Figure 2C) similar to those assembled from solution. Small differences (Figure 2C inset) in radius distribution arise here due to local variation in bead concentration and resulting μwheel sizes during assembly.

For convenience, we investigate aerosolized delivery within a 3D-printed human pediatric-scale mimic, fabricated at a length scale to model transport from the bronchiole into the alveoli (Figure 3A). To aid imaging, we fluorescently label the beads and then aerosolize them within droplets sprayed into the model using a commercially available nebulizer, dispersing broadly throughout (Figure 3B). Upon application of the rotating magnetic field, μwheels subsequently assemble and roll down the bronchial tube to the lower bronchus in ~5-10 min (Figure 3C). Here, a rotating field is applied to drive μwheels in the $+x$ direction to the ends of the channels where they accumulate (Figure 3D). While such transport capability in general is useful for delivering μwheels deeper into the lungs, specific targeting may be useful in localized diseases. For example, to avoid systemic delivery of chemotherapeutic agents and the associated side effects, inhaled delivery of drugs for lung cancer could prove a promising approach. Progress here however has been limited due to concerns over toxicity and potential damage to healthy tissues throughout the rest of the lung (38). An approach where chemotherapeutic agents are delivered via μwheels to tumor surfaces could significantly enhance treatment and minimize side effects not only for the rest of the body but within the rest of the lung as well. To demonstrate targeting and with the purpose of creating a bolus, we place a magnet near the end of the model inlet where, upon aerosolization and entering into the model, beads collect (Figure 3E). Upon removal of the magnet and with application of the weak rotating magnetic field, μwheels form (Figure 3F) and can be directly driven to a desired endpoint (Figure 3G and Figure 3H). Note here that because of the relatively large size of the aerosolized

building blocks, using fixed magnets for targeting deep in the lungs is not a workable strategy; in practice, magnets may not be required for targeting as beads can accumulate naturally at the upper end of larger scale systems due to their size.

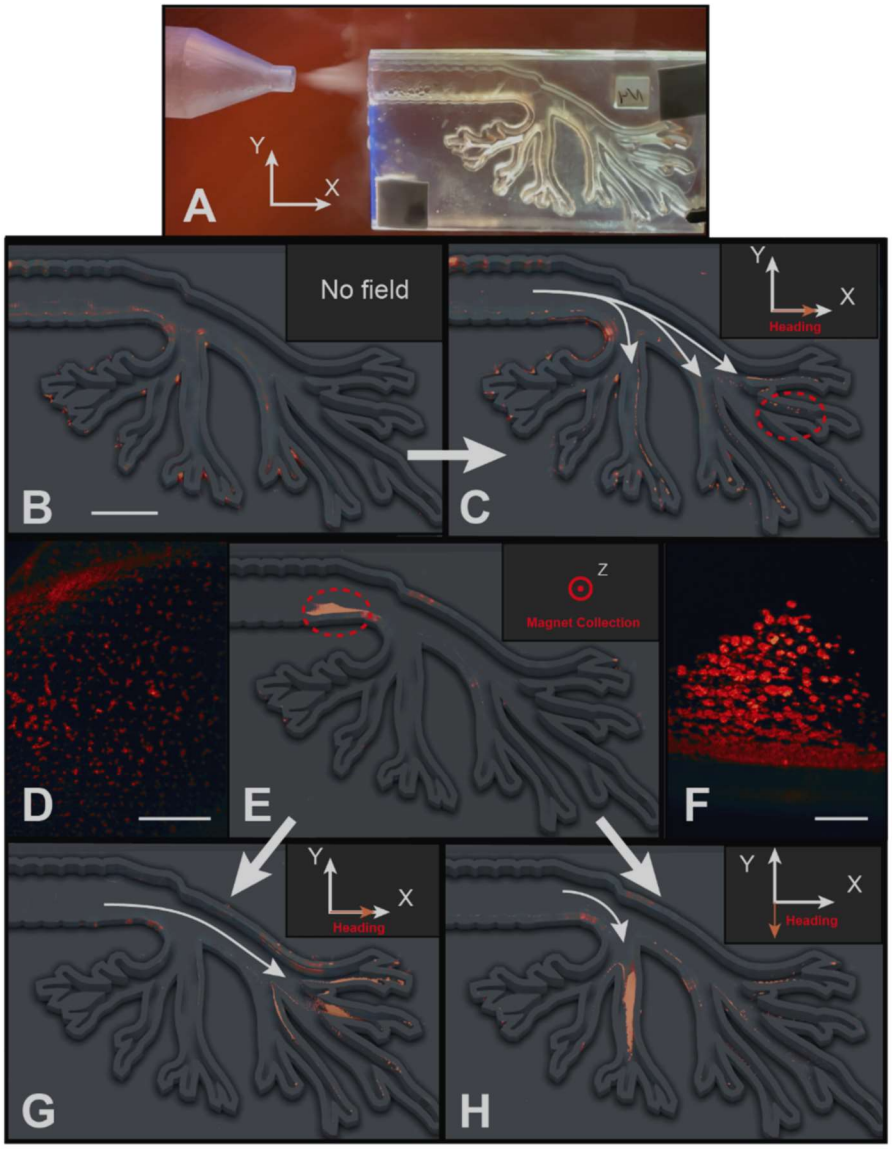

Figure 3.3 A) Aerosolization into 3D printed lung model. B) With illustration overlay, false color image of fluorescent, superparamagnetic beads dispersed throughout the model after aerosolization. Scale bar = 1 cm. C) Upon application of rotating magnetic field f = 40 Hz, B = 2.10 mT, axis of rotation $\hat{\boldsymbol{\Omega}} = [0, \cos(\pi/6), -1/2]$, μwheels form and D) travel down lung model pathways (Supplementary Video 3, scale bar = 1000 μm). Circled region in Fig 3C. E) For targeting, a permanent magnet can be used to capture aerosolized beads to form a bolus near the magnet. F) Upon magnet removal and with subsequent application of a weak rotating magnetic field, bolus μwheels (Supplementary Video 4, scale bar = 1000 μm) can be driven to desired branches. Circled region in Fig 3E. G) μWheels move deep into right branches with identical applied field to subfigure C. H) μWheels target the lower branches with applied field axis of rotation $\hat{\boldsymbol{\Omega}} = [\cos\left(\frac{\pi}{6}\right), 0, -\frac{1}{2}]$.

One interesting aspect of aerosolized delivery is that, because of the high concentration of μwheels that this creates, swarming in the resulting assemblies can be observed. In other studies, we have shown that such swarms can be actuated and controlled differently, giving rise to net μwheel transport optimized for dispersal, or travel up inclines, or simply for speed. For the purposes of the measurements of Figure 3, the lung model was fixed horizontally as gravity plays an important role in μwheel transport, providing a load force and wet friction with adjacent surfaces. As one would expect, rolling downhill increases translational velocities while travel up steep slopes slows μwheel movement; however, we have recently shown that, with appropriate field application, both individual and swarms of μwheels can continue to move up inclines as high as 80˚ (39). We note here also that viscosity can play a significant role; with $V \sim \omega$ for constant size μwheels, we expect $V \sim 1/\eta$ and a slowing down as viscosity increases. For travel from the bronchiole to the alveoli over 10's of cm, we expect μwheels to travel along the lower-viscosity sprayed fluid atop the higher-viscosity lung fluids already present while transport distances through the thicker mucus layer are significantly shorter and up to a few hundred μm (40). We have already demonstrated in previous studies the ability of these systems to deliver drug (7) and the incorporation of lung dispersants (41) to lower local viscosities is a potential strategy. Finally, and while we have chosen an approach with aerosolized droplets using a nebulizer for simplicity, we note that particle delivery could potentially be accomplished as a dry powder (42). Because the solid-phase building blocks are small enough and the particle size distribution well defined, once formulated, such an approach could provide advantages such as no need for propellants or more effective delivery for specific classes of drugs.

3.4 Conclusions

Here we have demonstrated an in-situ μbot assembly approach that enables the delivery of μbots of size up to 80 μm and power up to 60 fW into the airways of a model lung. Our experimental results show the feasibility of aerosolizing building blocks by partitioning individual colloidal beads into droplets that are small enough to be delivered deep down pulmonary channels. With application of a weak rotating magnetic field, these individual particles assemble into large μwheels capable of rapid translation through a model pulmonary network.

3.5 Methods

3.5.1 Magnetic Fields and Translation Studies

To create and control the applied rotating magnetic field, we use a home-built actuation system with coils and signal generation software which generates a circular rotating field (43). The z axis consists of one 50 mm i.d. 400 turn coil below the sample while the x and y axes have two 50 mm i.d. 400 turn coils all incorporated in the microscope stage (Olympus OpenStand). The field strength was varied from 2.1

mT (Figure 2C and Figure 3) to 3.4 mT (Figure 2C) to demonstrate the flexibility of the approach. The field rotation frequency was kept constant at 40 Hz. The circular rotating field was cambered, or tilted, 30° from the z-axis for easier μwheel visualization. For initial translation studies (Figure 2C), the sample chamber consisted of two square 22 mm glass cover slips of 0.17 mm thickness sandwiched with a rectangular gasket cut from double-sided tape (RP32 VHB™ tape, 3M, Maple, MN). To this, 4.5 μm diameter superparamagnetic beads (Dynabeads® M-450 Epoxy, Thermo Fisher, density = 1.5 g cm^{-3}) at an initial concentration of ~$4 \cdot 10^8$ beads ml^{-1} were diluted 200x with aqueous 0.2% sodium dodecyl sulfate (SDS) (Sigma-Aldrich) and added to the chamber. Videos were analyzed with custom open-source particle tracking software to measure rotation rates, radii, and velocities (44, 45). Stuck beads and monomers were excluded, defined as those with velocity and diameter less than 5 μm s^{-1} and 6.75 μm, respectively.

3.5.2 Bead-Laden Droplet Characterization

100 μl of Dynabeads® were fluorescently labeled by first adding 200 μl of aqueous 1 mg ml^{-1} rhodamine B solution and 700 μl of 0.2 wt% SDS aqueous solution. After 24 hr at room temperature, the solution was washed with 0.2 wt% SDS a total of 6x. Next, 100 μl of this solution was washed 3x with 0.1 wt% SDS and 5 vol% glycerine. The final solution was made after discarding the supernatant and adding 500 μl of 0.05 wt% SDS, 5 vol% glycerine, and 50 mg ml^{-1} of green food dye to increase the contrast and to form spherical droplets without air inclusions. The aerosol was created using the Pari LC® Sprint Reusable Nebulizer (MMD 3.5 μm) with supply air at 3 lpm. For quantification of droplet size, the aerosol was sprayed over a thin layer of Type B immersion oil on a glass slide for 1 min. A brightfield macroscan of ~2 mm^2 was taken with a 20x objective (Olympus IX81). This scan was performed using a stage loop where the camera and light source raster across a large area before being stitched together in software. Using threshold image analysis, the location and size of droplets and beads were determined. The data was then processed using a custom Matlab script to assign each bead to a specific droplet. Droplets below 0.5 μm in radius were not recorded due to image resolution limits.

3.5.3 Aerosolized μWheel Velocities

4 ml of Dynabeads® diluted with 0.2% SDS aqueous solution to a final concentration of $4 \cdot 10^6$ beads ml^{-1} was loaded into the nebulizer. The nebulizer was spaced 2 cm away and angled 45° towards a square 22 mm glass cover slip surrounded by a 5 mm high 3D printed retaining wall. The nebulizer was operated with a 3.5 lpm air supply until ~1 ml of solution was collected on the cover slip. The beads were then assembled into μwheels using the magnetic actuation system and microscope (Olympus OpenStand) with a field strength of 2.1 mT. For the control, 1 ml of the same solution was pipetted onto an identical cover

slip with retaining wall, then actuated with the same field conditions. The μwheel velocities and radii were measured using previously mentioned tracking software.

3.5.4 3D Printed Lung Model and Targeting

The 3D model was designed with a tracheal diameter of ~8 mm, corresponding to those measured for infants (46). The clear model was 3D printed (Form 3, FormLabs) and consisted of two halves which could be separated for viewing. A new model was printed for each experiment to avoid residual fluorescence staining. The model was first prepared by wetting with ~2 ml of 0.2% SDS solution. Next, fluorescently-labeled Dynabeads® were diluted to a concentration of $4 \cdot 10^7$ beads ml^{-1} with 0.2% SDS solution. The nebulizer nozzle was placed at the entrance of the model while 1 ml of the diluted Dynabeads® were aerosolized into the model with an air supply of 3.5 lpm for a total of 5 min. For experiments demonstrating targeting, a small permanent magnet was placed at the bottom of the model trachea, ~0.5 cm away from the first branch point. The measured field strength in the model at the point of collection was 130 mT.

For imaging, a macroscan using a TRITC filter (Olympus IX81) was taken after aerosolization to first characterize the initial distribution of beads throughout the model. For actuation, the device was placed on the microscope with magnetic actuation equipment (Olympus OpenStand). μWheels were assembled under an applied rotating field of 2.1 mT and actuated for 10 min for all experiments. The rolling direction of the μwheels was changed manually according to the targeted bronchial branch. Lastly, a second full macroscan of the device was performed to observe the movement of the fluorescently labeled beads after actuation.

3.6 Acknowledgements

C.J.Z, E.M.D., K.B.N., and D.W.M.M. acknowledge support from the National Institutes of Health under grants R21AI138214 and R01NS102465. We thank S. Inks, J.L. Wagner, T.A. Prileszky, and E.M. Furst for helpful discussions.

CHAPTER 4 COUPLING MAGNETIC TORQUE AND FORCE FOR COLLOIDAL MICROBOT ASSEMBLY AND MANIPULATION

Modified from a submitted paper.

Coy J. Zimmermann[15] , Andrew J. Petruska[16], Keith B. Neeves[17], David W.M. Marr[15]

4.1 Abstract

For targeted transport in the body, biomedical microbots (μbots) must move effectively in three-dimensional (3D) microenvironments. Swimming μbots translate via asymmetric or screw-like motions while rolling ones use friction with available surfaces to generate propulsive forces. We have previously shown that planar rotating magnetic fields assemble μm-scale superparamagnetic beads into circular μbots that roll along surfaces. In this, gravity is required to pull μbots near the surface; however, this is not necessarily practical in complex geometries. Here we show that rotating magnetic fields, in tandem with directional magnetic gradient forces, can be used to roll μbots on surfaces regardless of orientation. Simplifying implementation, we use a spinning permanent magnet to generate differing ratios of rotating and gradient fields, optimizing control for different environments. This use of a single magnetic actuator sidesteps the need for complex electromagnet or tandem field setups, removes requisite gravitational load forces, and enables μbot targeting in complex 3D biomimetic microenvironments.

4.2 Introduction

Microbots are a promising platform for biomedical applications as they can be readily directed to provide local mechanical action[4], [44], [103], [104], deliver drugs[105]–[108], can biodegrade[109]–[111] and swarm in a controllable fashion[112]–[114]. While microscale motility can be induced with chemicals[115], [116] and light[117]–[119], for biomedical applications, magnetic fields are favored due to their high biocompatibility[120] and deep tissue penetration[106]. Unlike magnetic materials that can be localized through surface functionality[121] or via magnetophoresis (MP) by simply placing a permanent magnet near the desired site, μbots are materials that can be actively directed at the microscale, enabling unique functionality including remote surgery[67], [122], precise delivery[123], [124], and cargo transport[12], [125]. Here we apply the simplicity of permanent magnet-based manipulation towards the assembly and actuation of μbot systems.

---

[15] Department of Chemical and Biological Engineering, Colorado School of Mines, Golden, CO, USA
[16] Department of Mechanical Engineering, Colorado School of Mines, Golden, CO, USA
[17] Departments of Bioengineering and Pediatrics, University of Colorado Denver | Anschutz Medical Campus, Aurora, CO

Magnetic μbots convert an external-field induced torque into movement. Swimming μbots[27], [126] locomote in the bulk fluid with non-reciprocal motion while rolling μbots use shear gradients near surfaces to move. Here, we focus on μwheels, a type of magnetic rolling μbot that reversibly assembles *in situ* from colloidal superparamagnetic beads upon application of a planar rotating magnetic field. μWheels are particularly suited for applications in the vasculature due to their ability to actively reconfigure. They share the speed advantages of larger systems and the access advantages of small systems, as they can assemble into large swarms to increase power and motility, then disassemble into their colloidal building blocks when the field is removed. We have shown that this reconfigurability enables unique actuation modes that enhance climbing, drug delivery[4], spreading, and velocity[114].

When brought near a surface with a load force, typically gravity but other forces have been demonstrated[10], [70], rolling μbots use a shear gradient near a surface boundary to move with velocity $V \propto \omega_b R$ where ω_b is the μbot angular velocity and R the bounding-circle radius[127]. Better control over the directionality and strength of the load force would enhance the ability of rolling μbots to traverse microenvironments that are tortuous and surfaces non-normal to gravity. In this work, we demonstrate a novel μbot actuation approach where the load is created through magnetic field gradients that complement the torque and translation-inducing rotating magnetic field.

Most magnetic μbots are driven by changing the direction of the bulk magnetic field in time which induces a torque. Field direction is simple to control with three independent electromagnet axes, often in a six-coil Helmholtz arrangement[45]. In a Helmholtz setup, the gradient of the field is negligible so no magnetophoresis is induced. μBots also have low field strength requirements (< 10 mT), so coils can be small, low power, and in a simple arrangement for small working volumes[96] as the field strength B scales with the inverse of the distance from the magnet cubed, $B \propto 1/r^3$. However, if full independent control of the gradient of the field is also desired, implementation increases in complexity, and a minimum of eight independent coils is required[46], [48], [52]. In general, the gradient component of the field induces a magnetophoretic force in magnetic material that is proportional to the inverse of the distance from the magnet to the fourth power, $F \propto 1/r^4$. Together, precise control of magnetophoresis for μbots requires larger magnetic actuation equipment with significant power and infrastructure requirements for human-scale use[128].

To translate, μwheels require a planar rotating field and an orthogonal load force to roll along a surface. We have previously shown that, with gravity alone, μwheels can roll up surfaces at angles up to 80°, demonstrating that only a small component of the load force needs to be in the direction of the surface[114], reducing the requirements for effective 3D μwheel translation. In effect, one requires only a rotating 3D field and one directional variable force to oppose gravity. A single rotating permanent magnet above the working volume can be used to simultaneously induce magnetophoretic forces to counteract gravity while still retaining the rotating field[129] . As the torque and force from a single magnet are

coupled and differ in scaling, the ratio of the magnitude of the torque and force can be readily altered by changing the distance between the magnet and sample. In this work, we demonstrate that by spinning and altering the distance of a nearby permanent magnet we can induce the assembly of superparamagnetic particles into µwheels with three distinct modes. At large magnet distances, magnetophoresis is low, gravity dominates, and µwheels roll along bottom surfaces (Fig. 1A). At medium distances, magnetophoresis can overcome weight allowing µbots to roll on inverted surfaces (Fig. 1B). At small distances, magnetophoresis dominates and µwheels can be collected and localized into a specified area. Once the magnet is removed, µwheels disassemble back into their constituent beads (Fig. 1C). With this simple actuation scheme, µwheels can move on all surfaces regardless of orientation with respect to gravity and navigate complex 3D biomimetic microenvironments.

4.3 Results

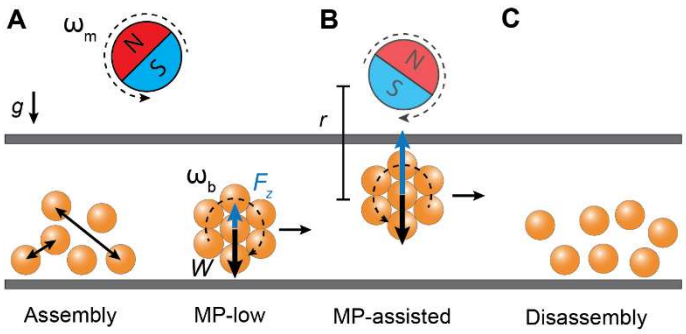

Figure 4.1 A single rotating permanent magnet can be used to create the simple fields required to A) assemble and spin µwheels while B) simultaneously supplying a load force opposite the direction of gravity. C) When the magnet is removed µwheels disassemble.

4.3.1 Coupled magnetic torque and force from a single spherical permanent magnet

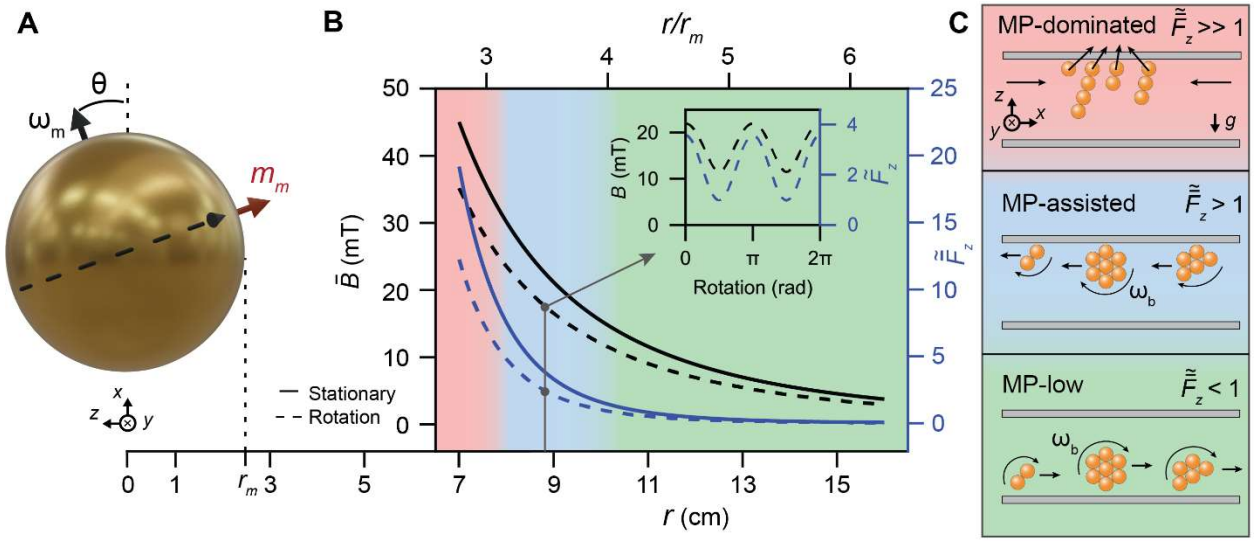

Figure 4.2 Magnetic field near a spherical permanent magnet. A) A spherical permanent magnet (r_m = 2.54 cm) has two poles with the moment $\mathbf{m_m}$ pointing through the north pole. The magnet is rotated around the angular velocity vector $\boldsymbol{\omega_m}$ which, for this study, is set perpendicular to $\mathbf{m_m}$. The camber angle θ measures the angle between the xy plane and $\boldsymbol{\omega_m}$ and is kept constant in this study at $\theta = 20°$. B) Left axis: The average field strength $\bar{B}$ a distance r away from $\mathbf{m_m}$. Right axis: The average normalized magnetophoretic force on a single bead in the z, or $\hat{\mathbf{r}}$ direction. $\bar{B} \propto 1/r^3$ and $\tilde{\bar{F}}_z \propto 1/r^7$. B inset) During rotation, B is at a maximum when m and r are parallel and drops by half when they are orthogonal. The magnetophoretic load drops by 4x when m and r are orthogonal ($r_z = 8.9\ cm$). C) Modes: Magnetophoresis (MP) low, MP-assisted, MP-dominated.

The field generated from a spherical permanent magnet (Fig. 2A) is described by the dipole equation[40]

$$\mathbf{B}(r) = \frac{\mu_0}{4\pi}\left[\frac{3(\mathbf{m_m}\cdot\mathbf{r})\mathbf{r}}{r^5} - \frac{\mathbf{m_m}}{r^3}\right] \tag{4.1}$$

where $\mathbf{B}$ is the magnetic flux density vector or magnetic field strength, μ_0 the magnetic permeability of free space, $\mathbf{r}$ the distance, r the norm of $\mathbf{r}$, and $\mathbf{m_m}$ the magnetic moment of the permanent magnet. Inspection of this equation reveals that the magnitude of the field scales with the inverse distance cubed, $B \propto 1/r^3$ (Fig 2B). Also, when the magnet moment $\mathbf{m_m}$ is in line with $\mathbf{r}$, the field is greatest as $\mathbf{m_m}\cdot\mathbf{r}$ is maximized. When $\mathbf{m_m}$ is orthogonal to $\mathbf{r}$, the field drops by half (Fig 2C); therefore, at a fixed $\mathbf{r}$ and as $\mathbf{m_m}$ is rotated around the angular velocity vector $\boldsymbol{\omega_m}$ (Fig 2A), an elliptical rotating field is generated. Note that for this study $\boldsymbol{\omega_m}$ is set to be orthogonal to $\mathbf{m_m}$ and $r_{xy} = 0$.

A torque is induced when a magnetic dipole $\mathbf{m_b}$ is misaligned with an external field $\mathbf{B}$ and is generally calculated via $\boldsymbol{\tau} = \mathbf{m_b} \times \mathbf{B}$. Since the colloidal beads that comprise μwheels are superparamagnetic, their moment is proportional to the local field strength, $\mathbf{m_b} = V_{bead}\chi\mathbf{B}/\mu_0$. For simplicity across all μwheel

shapes and sizes, the simple dipolar model is used here[130] where the bead moments are independent and are calculated only once based on the external field calculated from Eq. 1. When the magnet rotates with angular velocity $\boldsymbol{\omega_m}$, μwheels assemble into disks and rotate from the induced torque. The magnetization of the μwheel lags behind the magnetic field resulting in a magnetic memory torque[86] $\boldsymbol{\tau} = V_{bead} n \chi'' B^2 \hat{\boldsymbol{\omega}}_\mathbf{b} / \mu_0$ where χ'' is the imaginary magnetic susceptibility, n the number of beads, and $\hat{\boldsymbol{\omega}}_\mathbf{b}$ the field rotation unit vector at the μwheel. It follows that the torque on a μwheel is then proportional to the inverse distance from the magnet to the sixth power, $\tau \propto B^2 \propto 1/r^6$, a consequence of the bead moment being dependent on the local field strength. Note here that the rotation of the magnet $\boldsymbol{\omega_m}$ above the sample creates an opposite rotation direction at the sample $\boldsymbol{\omega_b}$, and thus an opposite μwheel rotation. In this study, the rotation rate is only 5 Hz enabling μwheels to rotate at the same rate as the field. When near a surface (< 2 μm)[70], μwheels roll with a heading unit vector $\hat{\mathbf{h}} = \hat{\boldsymbol{\omega}}_\mathbf{b} \times \hat{\mathbf{n}}$ where $\hat{\mathbf{n}}$ is the nearby surface unit normal.

The bead also experiences a magnetophoretic force $\mathbf{F} = \nabla(\mathbf{B} \cdot \mathbf{B}) V_{bead} \chi / \mu_0$. This force scales with the inverse of the distance to the seventh power $F \propto 1/r^7$ as the force is dependent on the shape of the field as well as the bead moment $\mathbf{m_b}$. We define a non-dimensional average force, $\tilde{\tilde{\mathbf{F}}} = \mathbf{F}/W$ where $\mathbf{F}$ is the magnetophoretic force on a single bead and W the buoyant weight force on a single bead. With this, $\tilde{\tilde{\mathbf{F}}} < 1$ when gravity dominates and $\tilde{\tilde{\mathbf{F}}} > 1$ when magnetophoresis is greater than the gravitational force. With a single magnetic dipole source, the field and force are coupled with the magnet distance r. The ratio between the field and force can be varied by changing the magnet distance r where the z, or against-gravity component, of the average normalized force $\tilde{\tilde{F}}_z$ is shown (Fig 1B). In this study, the magnet is placed above the sample, so that the largest component of the force is opposite the direction of gravity, allowing locomotive freedom and movement on inverted surfaces.

At small magnet distances ($r/r_m < 3$), $\tilde{\tilde{\mathbf{F}}} \gg 1$ and magnetophoresis dominates, resulting in an MP-dominated mode (Fig 2C) where locomotion due to the induced μwheel torque is insignificant and movement is based primarily on magnetophoresis. In confined systems, MP-dominated mode can be used to create a trapping area which concentrates magnetic material where the field is greatest. At medium distances ($3 < r/r_m < 4$), $\tilde{\tilde{F}}_z > 1$ and magnetophoresis is greater than the weight force. In this MP-assisted mode, μwheels lift off and roll on inverted surfaces. Upon rotation of the field, μwheels translate and use these new accessible surfaces to break symmetry and roll (Supplementary Video 1). The velocity of the μwheels due to the induced torque is much greater than the x-y component of the MP force, $\tilde{\tilde{F}}_{xy}$ (Supplemental Fig 1) and μwheels retain their maneuverability. Also, since μwheels move in the microenvironment, the variability of the field perpendicular to the magnet is less relevant as the working volume is smaller. Across a 16 cm^2 region, $\tilde{\tilde{F}}_z$ remains above 2 at $r_z = 8.3$ without having to reposition

the magnet. At large distances ($r/r_m > 4$), $\tilde{\tilde{F}}_z < 1$ and gravity dominates. µWheels use gravity as the requisite load force in this MP-low mode and retain their locomotion capabilities as previously reported with electromagnet actuation. Here, the rotating permanent magnet creates an elliptical rotating field with a slower field frequency (5 Hz), contrasting with previous studies with a circular field and higher frequency (40 Hz)[114], [127].

4.3.2 µWheel Manipulation

Due to the superparamagnetic nature of the constituent beads that form µwheels, the three actuation modes can be readily switched (Fig 3A-D, Supplemental Video 2). In the MP-dominated mode, beads collect in a trapping region against a wall where $\nabla\mathbf{B}$ is lowest. At a $\tilde{\tilde{F}}_{xy} = 6$, bead clusters initially travel towards the trapping point with a minimum velocity of ~40 µm/s. By rotating the magnet around the z axis, the direction of the moment vector can be changed, selecting the collection region without moving the magnet position in the *xy* plane (Fig 3A, B, E, F). This is possible due to the fixed 20° camber angle of the magnet which means $m_{xy} \neq 0$ in all orientations. When the field is removed, µwheels disassemble into their constituent beads (Fig 3C). In this system, this occurs at $r > 30$ cm. Note that disassembly is not required between actuation modes, but does affect µwheel size formation, as studied previously[114]. Additionally, collecting magnetic material in this way has been previously studied in detail due to its many applications in localized drug delivery and particle fractionization[131], [132].

µWheel trajectories were imaged, analyzed, and averaged over their entire length to characterize manipulation in the MP-assisted and MP-low modes in a horizontal glass parallel plate sample chamber. At high magnet separations, here $r_z = 11.3, 13.5$ cm, µwheels use gravity to roll on the bottom surface with positive velocity in the MP-low mode. In the MP-assisted mode, here $r_z = 8.3, 8.9$ cm, µwheels move to the top inverted surface and roll in the opposite direction with negative velocity (Fig 3H, Supplementary Video 1). Consistent with previous experimental results with electromagnets[36], µwheels with bounding-circle radius R roll with velocity $V \propto \omega_b R$. Here, all µwheels rotate in step with the field, leading to the linear $V \propto R$ behavior across all R due to the single field frequency reported here. The variable load force generated by the magnet does not strongly influence the traction under these experimental conditions (Fig 3I).

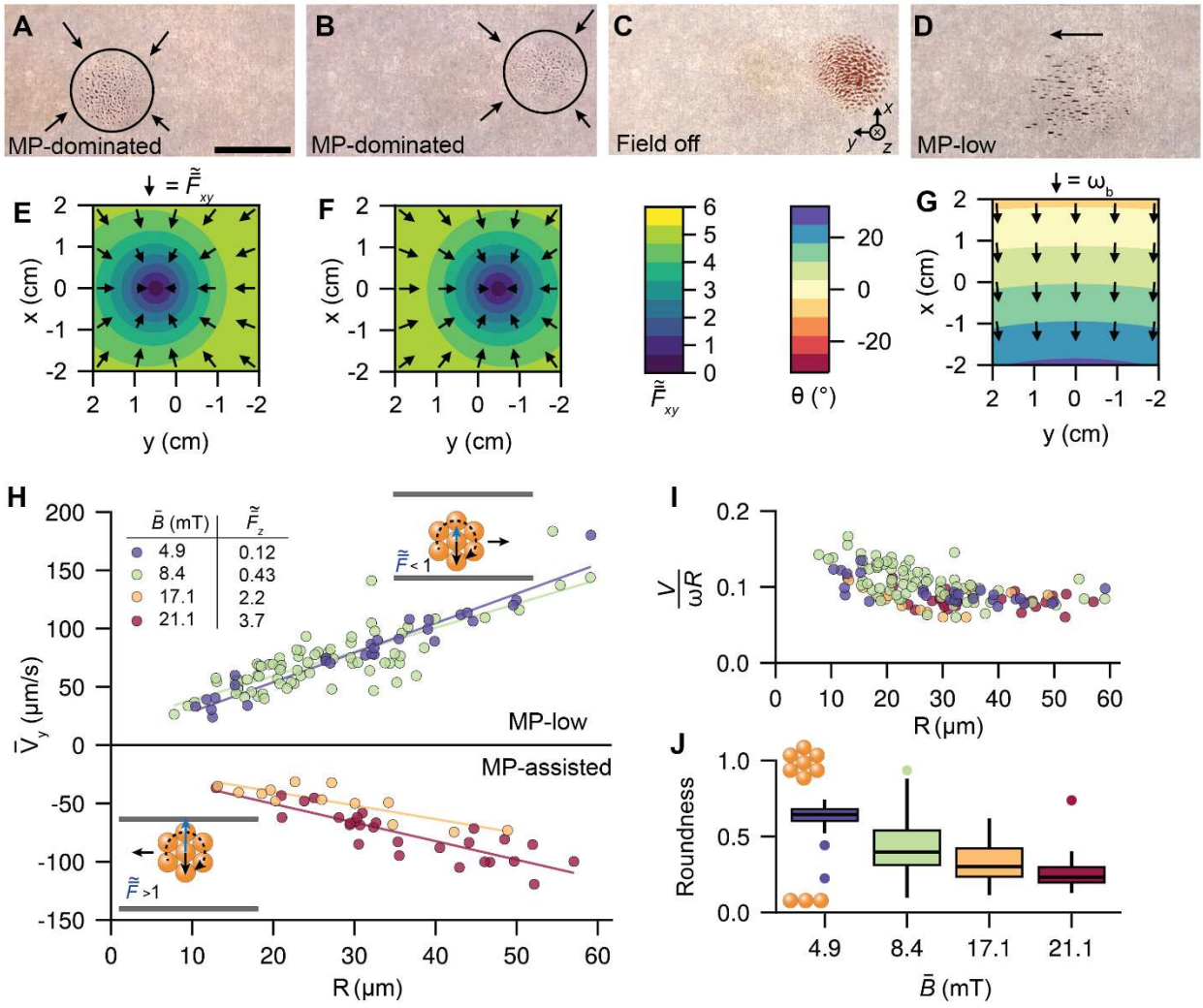

Figure 4.3 Permanent magnet μwheel manipulation. A,B) Beads are collected through magnetophoresis in the MP-dominated mode. C) When the field is removed ($r > 30$ cm) μwheels reversibly disassemble. D) μWheels roll in the MP-low mode. Scale for A-D = 0.55 cm. E,F) Force uniformity in the x-y plane at $r_z = 7.0$ cm, corresponding to images in A and B. Beads accumulate in the blue region where $\tilde{\tilde{F}}_{xy}$ is lowest. For E, $\hat{\mathbf{m}}_\mathbf{m} = [0, \sin(\pi/9), -\cos(\pi/9)]$ and for F, $\hat{\mathbf{m}}_\mathbf{m} = [0, -\sin(\pi/9), -\cos(\pi/9)]$. G) Uniformity of the rotational field in the x-y plane. Arrows correspond to $\hat{\boldsymbol{\omega}}_{\boldsymbol{xy}}$ of the field at each test point, while the color corresponds to the camber angle $\theta = \sin^{-1}(\hat{\omega}_z)$. H) Measured velocity and bounding-circle radius of μwheels in MP-assisted and MP-low modes at distances $r_z = 8.3, 8.9, 11.3, 13.5$ cm. I) Measured traction of μwheels across all field conditions and μwheel shapes. J) Measured roundness of μwheels where a value of 1 corresponds to a circular μwheel and a roundness of ~0.2 corresponds to a single bead wide chain.

The shape of the formed μwheels is determined by a balance between the drag torque due to the fluid and the magnetic torque. At lower field strengths, fluid drag overcomes these dipole-dipole attractions within the μwheel and the structure collapses into round, disk-like shapes. As the field strength increases, more linear μwheel conformations are preferred due to the alignment of the dipoles within the bead. To characterize this, we calculate a roundness according to $A \,/\, \sin(\theta)\,\pi R^2$ where A is the measured projected

area of the μwheel. Generally, roundness decreases as the field strength increases. The low rotation frequency combined with high field strengths generated by the permanent magnet enables low-roundness chains to form.

At high field strengths, these chains can get too large and exhibit instability and breakup, as reported elsewhere[89], [133]. The elliptical nature of the field used here likely increases this phenomenon, due to the dipole-dipole interaction strength halving twice every rotation. Due to the difficult nature of tracking these spurious trajectories, these unstable chains are not included in the data analysis. At low field strengths, we observe a "wobbling" behavior in large, round μwheels ($R > 30$ μm) at this low field frequency of 5 Hz, consistent with other experimental observations[34], suggesting that 5 Hz is in the transition region between "tumbling" and "rotating" modes of translation.

4.3.3 Magnetophoresis assisted movement enables full 3D rolling

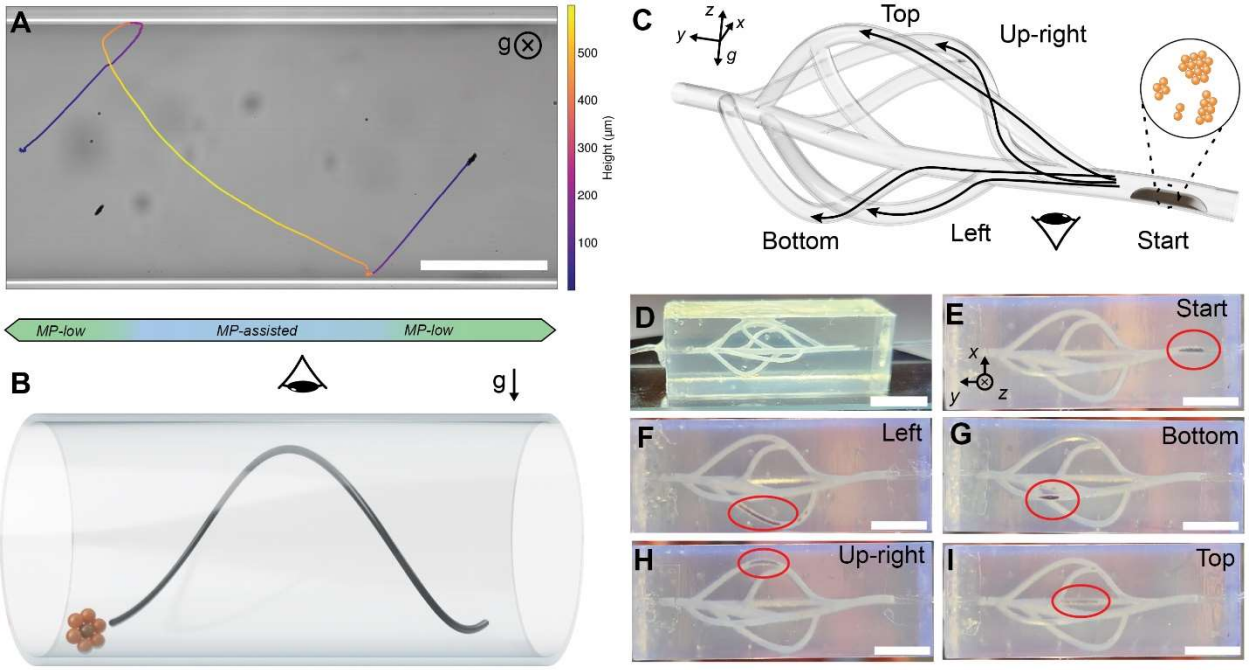

Figure 4.4 Magnetophoresis assistance enables gravity independent μwheel rolling. A) Individual μwheel performing a helical maneuver in a cylindrical capillary. The overlaid trajectory color is the height from the bottom of the cylinder in the normal, gravity direction. The MP-low mode is used for the beginning and end, while the MP-assisted mode is used in the middle to move on the top half of the capillary. Scale = 300 μm. B) Illustration demonstrating the programmed helical trajectory. C) Rendered CAD model of the bifurcating capillary network. D) Fabricated 3D-printed device. Scale = 1 cm. E) Snapshot of bead bolus at the start location. Scale = 0.75 cm. F) After targeting to the left capillary branch. G) After targeting to the bottom branch. H) After targeting to the upper-right branch. I) After targeting to the top branch.

To demonstrate complex μwheel maneuvers in 3D by switching actuation modes, a glass capillary is placed horizontally. Here, μwheels can use gravity as the requisite load force and move up the edges of

the capillary where the slope approaches 90° as observed in previous work[114]. When switching to MP-assisted mode however, the top half of a cylinder is now available for μwheel translation. Here, $\tilde{\tilde{F}}_z > 1$ and magnetophoresis is used as the requisite load force. To demonstrate switching between modes and the capability it provides, a helical maneuver is performed inside the capillary (Supplemental Video 3). When the μwheel reaches the edge of its locomotion capability in the MP-low mode, the mode is switched to the MP-assisted mode to move across the top half of the capillary.

To demonstrate that complex 3D biological networks are now traversable by μwheels, a 3D printed capillary network model was fabricated. In this, a bolus of beads was injected into the model and trapped at a designated start region with a small permanent magnet. In separate experiments, a μwheel swarm was driven into the four distinct capillary branches (Fig. 5, Supplemental Video 4). The left and bottom branches, located in plane and in the direction of gravity, are accessible solely using MP-low mode. When targeting branches like these, gravity is used as the requisite load force and the bottom capillary surfaces are used to move. The top branch, however, is directly above the main thoroughfare channel and requires a non-gravitational load force to access. Using the MP-assisted mode, the μwheel swarm is attracted to the top surface of the channel and rolls up and into the target branch. Lastly, the upper-right branch is accessible with either the MP-low or MP-assisted mode. Here, the MP-low mode was first used to steer into the branch followed by the MP-assisted mode to switch to the top surface and quickly climb the steeply inclined channel. Across all experiments, >90 % of the swarm was localized in the desired capillary branch. Swarm manipulation was also enhanced by using the previously studied "switchback" field pattern in which the μwheel size distribution was decreased and climbing ability increased[114]. After targeting a certain branch, the MP-dominated mode can be used to collect and concentrate the beads. This is particularly effective when the branch has a component in the direction towards the magnet. Otherwise, branches like the bottom branch have a natural collection behavior due to gravity collecting the beads.

4.4 Discussion

By combining a rotating bulk magnetic field with a controllable gradient force, the manipulation of colloidal μwheels in 3D geometries is greatly extended. This approach takes advantage of the superparamagnetic properties of μwheels, enabling reversible assembly and switching between modes. This property fits well with field-gradient techniques and allows prevention of large agglomerations which are especially important to avoid in biomedical applications. As a result, this approach is applicable to many of the complex 3D networks in the body including the pulmonary, circulatory, lymphatic, and excretory systems.

High field strengths directly increase the torque available to drive μbots. For paramagnetic μbots, $\tau \propto B^2$, further increasing the effect of field strength on μbot manipulation. This could prove useful for

increasing μbot translation rates by increasing the maximum rotation rate of μbots before they step-out of the field's rotation rate and enable movement through viscous and complex fluids in the body. For μwheels, higher fields favor eccentric shapes over perfect disks. These elliptical μwheels are more efficient; for a given number of beads, a higher bounding-circle radius μbot can be constructed. Since $V \propto \omega R$, the larger the radius, the faster the μwheel. Additionally, recent research has shown that eccentric, or slender, microrollers reduce out-of-plane rotational flows and perform better in confined geometries[29].

Due to the simple fields required for μwheel assembly and movement, a single rotating permanent magnet can readily supply the necessary fields. Since μwheels only require a small load force component into a nearby surface and can climb extreme slopes[114], the magnet only needs to be placed above the working volume to counteract gravity while simultaneously applying a bulk rotating field. While swimming μbots would still rotate in the presence of the rotating field, the locomotion direction for swimming μbots is perpendicular to their rotation. Consequently, they are more sensitive to the orientation of the local field than μwheels, which keep rolling as they tilt[36], [134] . Additionally, magnetophoresis would only increase μbot translation when the force vector is in the same direction as locomotion and likely would hinder the intended manipulation.

The permanent magnet actuator in this study is simple and does not require additional scaling up for human use, unlike electromagnetic systems typically used for μbot research. The 5 cm diameter spherical magnet used here is suited for MP-assisted use 7-9.5 cm (up to ~25 mT) and MP-low use up to 15 cm (2 mT). This working distance allows penetration into most deep regions of the body. If needed for specific applications, a 10 cm magnet would project its field twice as far but, at a given field magnitude, the gradient would be decreased due to the homothetic property of magnetic objects[40]. While the use of a permanent magnet for μbot manipulation has been previously studied[55], [134], [135], its application for assembly and full 3D manipulation of rolling μbots has not been reported. These previous studies however have demonstrated how such magnets can be affixed to a robotic arm for positioning over the entire body[55] or can be spun in fluid for >100 Hz rotation rates[135].

4.5 Conclusions

Simultaneous use of the torque and force components of a magnetic field enables μwheels to move on previously inaccessible inverted surfaces. Microwheel swarms can switch modes between collection, inverted translation, and gravity assisted translation by simply changing the balance between magnetic bulk and gradient fields. Such coupled force and torque actuation is particularly fitted to rolling μbots as the requisite load force is low and perpendicular to the rotation direction. With this approach, full μwheel navigation is now possible through 3D networks regardless of the orientation with respect to gravity. Implementation of this scheme was significantly simplified using a single rotating permanent magnet with

three degrees of freedom, sidestepping the need for prohibitively large human-scale electromagnet systems.

4.6 Methods

4.6.1 Magnetic Fields

The magnetic field generated by a spherical permanent magnet is perfectly described by the dipole equation (Eq 1) outside the magnet body[40]. The moment of a hard permanent magnet is calculated by $\mathbf{m_m} = B_r V/\mu_0$ with B_r the residual flux density, V the magnet volume, and μ_0 the vacuum magnetic permeability. The moment $\mathbf{m_m}$, by convention, points from the magnet center through its north pole. The magnet used in this study is a neodymium sphere of diameter 50.8 mm and $Br = 14800$ Gauss (N52 sphere, Applied Magnets, Plano TX, USA).

The moment of a superparamagnetic bead is assumed to be a soft magnet below saturation and is calculated by $\mathbf{m_b} = V_{bead}\chi\mathbf{H_0}$ where V_{bead} is the bead volume, χ the magnetic susceptibility, and $\mathbf{H_0}$ the external magnetic induction field. In this study, the magnetization of the medium (water) is assumed to be negligible so $\mathbf{B} = \mu_0\mathbf{H}$. The beads used in this study are M-450 Dynabeads (Thermo Fisher) with a reported magnetic susceptibility[136] of $\chi_m = 1.63$.

4.6.2 3D printed magnet actuator

A custom robotic actuator was designed with three degrees of freedom (DoF) to create the necessary fields for gradient assisted microbot rolling (software Fusion 360, Autodesk). The body of the device was 3D-printed (Prusa Mk3s+, Prusa Research, Prague, Czech Republic) in polyethylene terephthalate glycol plastic (Hatchbox 3D, Pomona, CA) with specialty parts purchased from McMaster-Carr (Douglasville, GA). The use of metal in the device, especially close to the magnet, was minimized to prevent eddy currents. The motors used were brushless dual shaft motors (D5065 270KV, ODrive Robotics) with an encoder (CUI AMT102-V, ODrive Robotics) mounted on each secondary shaft. Control was performed with an ODrive v3.6 board that interfaces with Python and allows the motors to be precisely controlled with position and velocity feedback control. The device consists of an upper portion that rotates and directs the rolling direction of the magnet (1st and 2nd DoF) and a lower portion that moves the sample and microscopy train to a prescribed distance from the magnet (3rd DoF).

Only three DoF are required for the necessary magnet movements. First, the magnet can spin around a given angular velocity vector $\hat{\boldsymbol{\omega}}_\mathbf{m}$ up to 20 Hz. The spherical permanent magnet is securely fixed in a 3D printed holder with a shaft in line with $\hat{\boldsymbol{\omega}}_\mathbf{m}$. For this study, the magnet moment $\hat{\boldsymbol{m}}_{\boldsymbol{m}}$ was arranged perpendicular with $\hat{\boldsymbol{\omega}}_\mathbf{m}$ by aligning the magnet poles orthogonal to the shaft. This shaft is rotated using a pulley and belt system with a nearby motor. Second, $\hat{\boldsymbol{\omega}}_\mathbf{m}$ can be moved 360° in the xy plane to set the rolling direction. This is performed by affixing the magnet rotator to a large 3D printed gear assembly

which can rotate to a specific position with software input. Optionally, the z component of $\hat{\boldsymbol{\omega}}_{\mathbf{m}}$, which sets the camber angle, can be changed by varying the mounting angle of the rotator to this 3D printed gear with a 3D printed insert. Third, the sample distance to the magnet can be varied to change the magnetic field and force strength. This is performed by moving the lower portion with the sample and microscopy train towards or away from the upper portion with the magnet with a motor-driven belt.

The lower portion is modular and can be switched between a microscope mode for micro-scale imaging or a macro mode that supports a smartphone. The microscope consists of a 10x objective (Nikon) mounted to a high-speed camera (pco.panda 4.2, Excelitas PCO GmbH) that is moved and focused with a 3-axis linear translation stage (460-XYZ, Newport). An LED light source with collimator (LEDD1B with COP1-A, ThorLabs) is mounted to the left of the sample and light is directed through the sample to the microscope using a mirror mounted at 45˚. For macro mode, the microscope is replaced with a 3D-printed holder for a smartphone (S22+, Samsung). In this mode, the LED light source is removed and the 45˚ mirrors replaced with a white backsplash for enhanced imaging contrast.

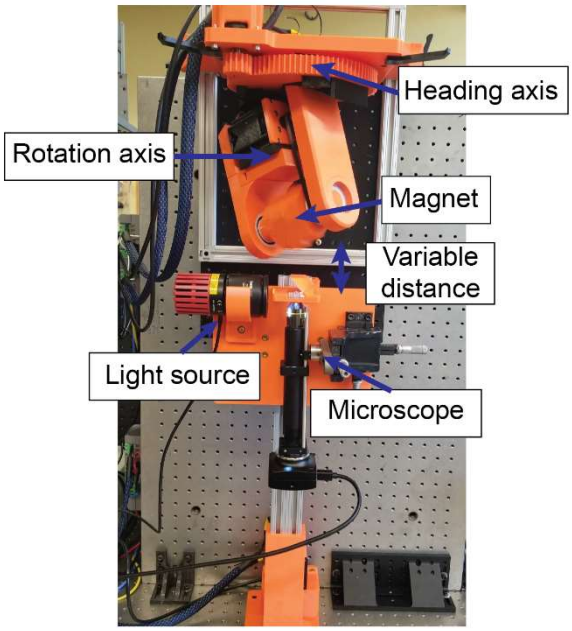

Figure 4.5 Rotating permanent magnet apparatus. The top construction contains a 2” N52 spherical permanent magnet capable of rotation rates up to 20 Hz and heading angles 0° to 360°. The bottom construction moves the sample and microscopy train on a linear axis towards and away from the rotating magnet.

4.6.3 Macro-scale µwheel swarm demonstration

A sample well was constructed using double sided tape (3M VHB Tape GPH-060GF) placed around the edges of a 1 x 3” glass slide. Approximately 2 µL of 4.5 µm beads with initial concentration of $4 * 10^8$ beads/mL (Dynabeads® M-450 Epoxy, Thermo Fisher) were diluted 100x in 0.2 wt % sodium

dodecyl sulfate (SDS) (Sigma-Aldrich). This was added to the reservoir and the remainder of the volume was filled with 0.2 wt % SDS solution. Videos were recorded using the macro-imaging mode from below.

4.6.4 Microwheel velocities

A sample chamber was constructed by cutting an approximately 1 x 1.5 cm rectangle in double sided tape (3M VHB Tape GPH-060GF) and placing it on a 1 x 3" glass slide. Approximately 60 µL of 500x diluted 4.5 µm beads (Dynabeads® M-450 Epoxy, Thermo Fisher) in 0.2 wt % sodium dodecyl sulfate (SDS) (Sigma-Aldrich) was added to the reservoir and covered with a square 22 mm glass cover slip. The sample was placed in the holder and imaged using a custom microscope (see 3D printed magnetic actuator methods). Videos of µwheels rolling at each experimental condition were recorded and then analyzed using custom µbot tracking software written in Julia[137].

4.6.5 Helical motion in a cylindrical capillary

A glass capillary (OD 1000 µm and ID 580 µm) was suspended over a glass slide with a 3D printed enclosure filled with dimethyl sulfoxide (DMSO) (Sigma-Aldrich). The capillary was filled with approximately 1 µL of 500x diluted 4.5 µm Dynabeads® in 0.2 wt % SDS in DMSO. The DMSO (refractive index = 1.479) enabled clear viewing through the round capillary with minimal refraction at the curved edges. The custom microscope (see Methods) was used to record µwheel movements with the focus fixed to show out of plane movements.

4.6.6 Capillary Network Targeting

A 3D biomimetic capillary network model was designed in CAD software Fusion 360 with four distinct branches off a thoroughfare channel. The model was 3D printed using stereolithography (Form 3, FormLabs) in clear plastic. After removing support material and washing thoroughly with isopropyl alcohol (IPA) (Sigma-Aldrich), the inlets were plumbed with 0.01″ ID by 0.030″ OD clear Tygon® tubing (Cole Parmer) and fixed in place with two-part epoxy. The outside surfaces of the devices were sprayed with three coats of glossy clear paint (249117 Gloss Clear, Rust-Oleum) to increase transparency. After curing, the internal channels were subsequently rinsed with 1 mL of IPA, 1 mL of deionized water, and 1 mL of 0.2 wt% SDS. Then, 0.3 mL of 30x diluted 4.5 um Dynabeads® was loaded while a permanent magnet was simultaneously placed near the inlet junction. The device was placed in the sample holder of the magnetic actuator in macro-photography mode. Videos were recorded in the macro-imaging mode from below, showing the progress of the micro-swarm throughout magnetic targeting.

4.7 Acknowledgments

The authors thank Y. Gao for the insightful discussion and acknowledge support from the National Institutes of Health under grants R21AI138214 and R01NS102465.

CHAPTER 5 MICROTRACKER.JL: A JULIA PACKAGE FOR MICROBOT RESEARCH

Modified from a submitted paper.

Coy J. Zimmermann[18], Keith B. Neeves[19], David W. M. Marr[18]

5.1 Summary

Microbots are active matter capable of performing remote mechanical work at the micro-scale. They are of particular interest for biomedical applications and drug delivery due to their ability to target and provide local mechanical action[114]. However, at the micron scale, traditional propulsion methods such as propellors do not work. Instead, microbot designs mimic nature, like bacterial flagella that corkscrew through fluid[26] or white blood cells that roll on vascular surfaces[65]. The rapidly-expanding field of microrobotics is focused on researching new structures, fabrication techniques, and actuation methods, all amplified by the recent adoption of nano-scale 3d printing techniques[12] and human-scale remote magnetic actuation equipment[8].

Current research requires quantitative measurements of the velocity, rotation rate, and size of large numbers of individual microbots under varying actuation and environmental conditions. Efficient software tools are needed to quickly and easily process this large amount of experimental data with which, microbot design can be further informed to increase the locomotion efficiency and suitability for a variety of fluidic environments.

5.2 Statement of Need

MicroTracker.jl is a Julia[137] package for tracking and analyzing microbots in optical microscopy videos. The package and accompanying documentation allows researchers to go from an array of experiments at various conditions to useful summary statistics, interactive data visualization, and publication-ready figures that enable quick informed decisions on future microbot design. Working alongside the commonly used image analysis tool, ImageJ[138], to segment images into particles, MicroTracker.jl tracks the velocity, size, shape, and rotation rate of hundreds of microbots at once across multiple videos at various experimental conditions.

This is performed by linking individual segmented particle data from each video frame into coherent trajectories using established methods[139], [140]. Once linked, the velocity and size trajectory of each microbot can be extracted given microscope parameters frames/second and microns/pixel. Various

[18] Department of Chemical and Biological Engineering, Colorado School of Mines, Golden, CO, USA
[19] Departments of Bioengineering and Pediatrics, University of Colorado Denver | Anschutz Medical Campus, Aurora, CO

functions are included in the analysis pipeline to reduce error, including clipping data where the microbot is occluded near the edge of the frame. Then, the time-data is collapsed and summarized to characterize and compare microbots. Fourier analysis is used to extract the mean rotation rate from periodic changes in the microbot shape. Together, insights can be easily extracted from large experimental designs, enabling high-throughput data analysis.

MicroTracker.jl also features an interactive microbot visualizer that displays the velocity, size, and frequency data along with the annotated trajectory [Fig1]. Sliders and dropdown menus enable the user to scan through each individual video, microbot, and time point. This level of interactivity is critical for analyzing how a given microbot design moves under given experimental conditions. Additionally, with thoughtful naming of microscopy video files with their experimental conditions, MicroTracker.jl can automatically generate publication-ready plots with the help of Julia plotting libraries[141] that summarize the entire experimental sets. Together, these tools allow researchers to make insights at both the individual microbot and condition-wide levels.

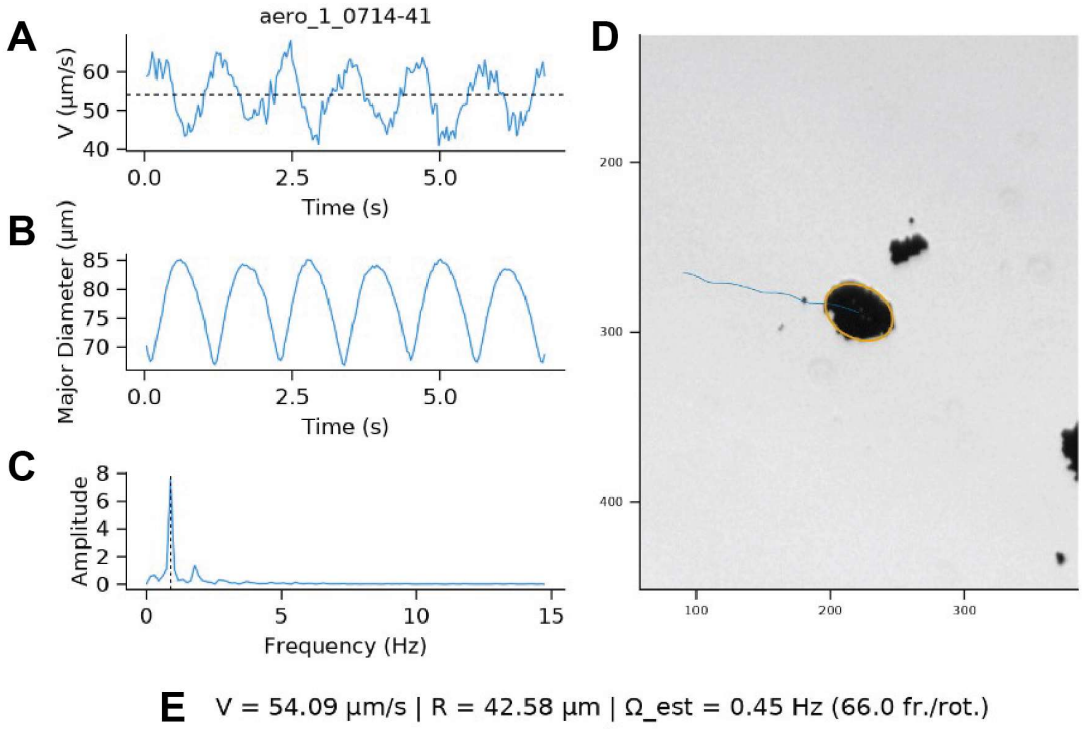

Figure 5.1 Interactive microbot visualizer from MicroTracker.jl. A) The instantaneous velocity profile along with the mean velocity (dotted line). B) The major diameter, or bounding-circle diameter, profile is plotted along with its C) Fourier transform to identify the rotation rate of a microwheel. D) A snapshot of the microscopy video along with a drawn trajectory and fit ellipse for the chosen microbot. E) Summary statistics across the entire trajectory. Includes the average velocity, bounding-circle radius, and identified rotation rate from the Fourier analysis.

Tracking of particles in microscopy video has previously been performed either manually through image processing software[99] or in an automated fashion with particle tracking software such as TrackMate[142] or Trackpy[140]. These software were primarily designed for tracking spherical uniform particles and use methods such as the Laplacian of Gaussian that determine the centroid of a Gaussian feature of a certain size. However, these detectors can be ineffective with microbots as they can vary widely in size and shape. MicroTracker.jl allows for size, shape, and rotation rate tracking of microbots which regularly enter and leave the video frame and is a open-source package catered specifically for microrobotic research.

A collection of Pluto.jl[143] notebooks are included with this package to provide a simple template and tutorial for users with limited coding experience. Additionally, a detailed tutorial on how to prepare microscopy video with ImageJ for use with MicroTracker.jl is included in the documentation along with a sample ImageJ macro for easy batch processing.

Multiple publications that make use of tools in MicroTracker.jl have been published or are in preparation but their scientific contribution is unique and independent of this package. These include studies of microbots for use in the vasculature[114], lungs[127], gastrointestinal system[144], and at the air water interface[145].

5.3 Use of MicroTracker.jl in this thesis

A large portion of the work detailed in this thesis was made possible by the tools developed in MicroTracker.jl. In Chapter 2, the velocity and rotation measurements of μwheels in Figure 2.2, Figure 2.3, and Figure 2.4 were performed using an early version of this software written in Python and the corresponding library trackpy[98]. The ability to rapidly measure individual microwheels in a large swarm as it moved was pivotal in extracting meaningful statistical representations of swarm behavior. In Chapter 3, the data acquisition for Figure 3.1 and Figure 3.2 was also enabled with the particle tracking tools developed as part of this software. Lastly, in Chapter 4, the microwheel data in Figure 4.3 was extracted and analyzed with MicroTracker.jl. The trajectory drawing and tracking of a microwheel moving in 3D was also performed using these tools in Figure 4.4.

5.4 Acknowledgements

C.J.Z. and D.W.M.M acknowledge support from the National Institutes of Health under grants R01NS102465 and R21AI138214.

CHAPTER 6 CONCLUSION AND RECOMMENDATIONS

6.1 Summary

While there has been an explosion of research into various aspects of biomedical microbot design and usage, careful study of microbot locomotion in 3D is needed. Swimming microbots are capable of full 3D movement yet are slow for their size. We believe the most versatile and promising technology is roller based; including microwheels which are reversibly assembled from the bottom up with paramagnetic building blocks. The research presented here has broad implications, marking a significant step in fully realizing minimally invasive treatments performed safely and remotely at the microscale.

In Chapter 2, we detail a microwheel swarm platform that can be readily switched and tuned for targeting, penetration, climbing, or spreading. The individual microwheels that comprise these swarms are studied at increasingly steep inclines and swarm-mode specific size distributions, or "fingerprints", are uncovered. Together, these yield useful insights including the discovery that microwheels continue to locomote with little load force up extreme slopes and modifying the size-distribution directly determines the swarm behavior. Additionally, a simple model for swarm targeting in pseudo-3D biological networks is presented, allowing predictive quantification of microwheel targeting capability in arbitrary environments.

In Chapter 3, individual microwheel building blocks are successfully aerosolized and subsequently reassembled in a liquid film. Commercially available nebulizers, with tuned droplet sizes optimal for lung delivery, are modified to carry drug-laden bead payloads. This bead-laden aerosol is sprayed into 3D printed lung models to demonstrate two delivery modes: lung-wide and targeted. In the lung-wide mode, beads are distributed throughout the lungs and subsequently assembled to roll deeper and reach areas inaccessible to traditional aerosols. This technique could prove useful for treating pulmonary diseases such as cystic fibrosis which are recalcitrant to traditional drug delivery techniques. In the targeted mode, a secondary permanent magnet collects bead-laden droplets at a pulmonary branch point, enabling targeted directed movement of microwheel swarms to a specific area. This research is promising for highly targeted delivery of harmful but necessary chemotherapy agents for lung cancer.

In Chapter 4, a coupled magnetic force and torque technique is developed to greatly extend the rolling surfaces available to microwheels. Since microwheels assemble and roll with simple rotating fields and require low load forces orthogonal to their heading direction, a single rotating permanent magnet can supply the necessary fields for movement on all surfaces regardless of their orientation with respect to gravity. The ratio between the magnetic force and torque can be modified by simply changing the magnet distance and results in three distinct actuation modes that complement the swarm modes detailed in Chapter 2. Together, microwheel swarms are successfully demonstrated targeting in complex bifurcating biological network models.

In Chapter 5, an original open-source software package for microbot tracking is introduced. Its functionality is pivotal in the completion of the work in this thesis and enabled high-throughput analysis of microwheels translating at a variety of experimental conditions. This package is MIT licensed to promote future collaboration across research groups for easy and efficient microbot analysis.

The work presented in this thesis is part of a large research effort to realize the advantages of microbots as a biomedical intervention platform. The following recommendations detail what future work is needed for delivery and actuation of microwheels in increasingly complex animal models and eventual clinical use.

6.2 Outlook and Recommendations

6.2.1 Human-scale permanent magnet actuator

The work in Chapter 4 can be easily extended to create a single permanent magnet actuator that can be used anywhere on the body. Robotic arms with permanent magnet actuators have been reported in detail elsewhere but haven't addressed their application to paramagnetic microbots like microwheels. Additionally, minimal scale-up is needed as the commercially available 2" diameter magnet used in chapter 4 is adequate for use deep in the body. With simple actuators and field techniques like this, the large infrastructure barrier for clinical use can be sidestepped. Additionally, increasingly large models can be used and microbot research would no longer be limited by the magnetic actuation working volume.

6.2.2 Microwheel movement in thin liquid films

Recent work in our group has discovered that microwheels do not require a solid surface to roll and instead can use air/liquid interfaces to break flow symmetry. Another curious finding of this study is that the movement direction of a rotating microwheel near this air/liquid interface switches. Therefore, it follows that in a liquid film microwheels would move in a single direction no matter if they're breaking symmetry by being near the air or solid interfaces. Additionally, if the film is small enough, microwheel velocities would increase due to the decreased total fluid drag in the film. This is of particular interest for lung applications where these interfaces are common. A full study investigating this behavior is needed to further understand microwheel locomotion in the actual lung.

6.2.3 Viscous and non-Newtonian environments

The torque available to a microwheel is proportional to the square of the magnetic field strength. Using the high (~30 mT) field strengths now accessible due to the use of a permanent magnet actuator presented in Chapter 4, environments previously inaccessible due to insufficient microwheel torque are now available. The body contains a plethora of fluids with various viscosities and rheological properties that are difficult to navigate with the low field strengths created by typical electromagnet coil systems.

With this, fundamental studies investigating microbot movement in these challenging environments are now accessible. This is particularly impactful for translation in diseased lung environments such as those with cystic fibrosis, where viscous mucous and bacterial biofilms are recalcitrant to traditional drug delivery techniques. Here, microbots present a promising solution to current treatment methods.

6.2.4 Movement in flow

The recent explosion in microbot research has resulted in large progress in microbot movement in flow which is particularly important for vascular applications. Others have shown two approaches that work; highly susceptible ferromagnetic bots that are dense and quick enough to move counter-flow[65], and tandem ultrasound and magnetic fields to pull microbots close to a wall[70]. With the coupled force and torque technique detailed in Chapter 4, it follows that the magnetophoretic force could retain microwheel contact near the low-flow region of the capillary wall enabling microwheel movement in flow. Additionally, the higher torque available to microwheels from permanent magnet actuation results in quicker velocities, potentially enhancing mobility in these challenging environments.

6.2.5 Microwheel swarms in confined geometries

Recent research elsewhere has reported that slender rolling microbots are more effective at moving in confined geometries than their spherical counterparts due to decreased rotational flows[29]. As microwheels are assembled into planar, slender configurations, they would likely excel in this environment. The swarm modes, developed in Chapter 2, simply break apart large microwheels into a desired size distribution. The switchback or flipping modes, which create the smallest microwheels, could potentially create microwheels with the necessary size for directed movement in small capillaries. In Chapter 4, the switchback mode was used to enhance swarm locomotion inside biological network models, yet these networks had a relatively large inner diameter (500 um). Vessels in the body can be as small as 8 um [146] so further study of swarm breakup dynamics at this length scale is needed for future in vivo use.

6.2.6 Magnetic field driving frequency optimization

The torque induced on a microwheel can be modeled by $\tau \propto \chi''$ where χ'' is the imaginary magnetic susceptibility[86]. The value of this susceptibility is primarily dependent on the magnetic field frequency. Additionally convoluting the problem, the opposing rotational drag torque on a microwheel is dependent on its shape and size, resulting in a field and medium dependent step out frequency. A fundamental study of the frequency response of microwheels is needed to optimize microwheel swarm velocities in biological environments. For example, a flipping-mode swarm would be comprised of smaller microwheels which would have a higher step-out frequency in a given medium. Therefore, a higher driving frequency would be optimal when using the flipping swarm mode. Additionally, the software

presented in Chapter 5 greatly improves microbot analysis throughput and would enable a comprehensive experimental study of this size.

REFERENCES

[1] T. Brody, "Dose Modification and Dose Titration," in *FDA's Drug Review Process and the Package Label*, Elsevier, 2018, pp. 101–151. Accessed: Dec. 11, 2019. [Online]. Available: https://linkinghub.elsevier.com/retrieve/pii/B978012814647700004X

[2] H. Olson *et al.*, "Concordance of the Toxicity of Pharmaceuticals in Humans and in Animals," *Regul. Toxicol. Pharmacol.*, vol. 32, no. 1, pp. 56–67, Aug. 2000, doi: 10.1006/rtph.2000.1399.

[3] X.-Z. Chen *et al.*, "Recent developments in magnetically driven micro- and nanorobots," *Appl. Mater. Today*, vol. 9, pp. 37–48, Dec. 2017, doi: 10.1016/j.apmt.2017.04.006.

[4] T. O. Tasci *et al.*, "Enhanced Fibrinolysis with Magnetically Powered Colloidal Microwheels," *Small*, vol. 13, no. 36, p. 1700954, Sep. 2017, doi: 10.1002/smll.201700954.

[5] J. Gilbert, "The Use of Nanorobotics to Treat Cystic Fibrosis".

[6] M. Hoop *et al.*, "Magnetically Driven Silver-Coated Nanocoils for Efficient Bacterial Contact Killing," *Adv. Funct. Mater.*, vol. 26, no. 7, pp. 1063–1069, Feb. 2016, doi: 10.1002/adfm.201504463.

[7] J. Han *et al.*, "Hybrid-Actuating Macrophage-Based Microrobots for Active Cancer Therapy," *Sci. Rep.*, vol. 6, no. 1, Sep. 2016, doi: 10.1038/srep28717.

[8] B. Wang, K. Kostarelos, B. J. Nelson, and L. Zhang, "Trends in Micro-/Nanorobotics: Materials Development, Actuation, Localization, and System Integration for Biomedical Applications," *Adv. Mater.*, vol. 33, no. 4, p. 2002047, Jan. 2021, doi: 10.1002/adma.202002047.

[9] E. M. Purcell, "Life at low Reynolds number," *Am. J. Phys.*, 2014.

[10] Daniel Ahmed, T. Baasch, N. Blondel, N. Läubli, J. Dual, and B. J. Nelson, "Neutrophil-inspired propulsion in a combined acoustic and magnetic field," *Nat. Commun.*, vol. 8, no. 1, p. 770, Dec. 2017, doi: 10.1038/s41467-017-00845-5.

[11] F. Qiu *et al.*, "Noncytotoxic artificial bacterial flagella fabricated from biocompatible ORMOCOMP and iron coating," *J Mater Chem B*, vol. 2, no. 4, pp. 357–362, 2014, doi: 10.1039/C3TB20840K.

[12] S. Jeon *et al.*, "Magnetically actuated microrobots as a platform for stem cell transplantation," *Sci. Robot.*, vol. 4, no. 30, p. eaav4317, May 2019, doi: 10.1126/scirobotics.aav4317.

[13] W. Gao *et al.*, "Cargo-Towing Fuel-Free Magnetic Nanoswimmers for Targeted Drug Delivery," *Small*, vol. 8, no. 3, pp. 460–467, Feb. 2012, doi: 10.1002/smll.201101909.

[14] P. Erkoc, I. C. Yasa, H. Ceylan, O. Yasa, Y. Alapan, and M. Sitti, "Mobile Microrobots for Active Therapeutic Delivery," *Adv. Ther.*, p. 1800064, Oct. 2018.

[15] H.-W. Huang, M. S. Sakar, A. J. Petruska, S. Pané, and B. J. Nelson, "Soft micromachines with programmable motility and morphology," *Nat. Commun.*, vol. 7, no. 1, p. 12263, Nov. 2016, doi: 10.1038/ncomms12263.

[16] Conghui Liu, Tailin Xu, Li-Ping Xu, and Xueji Zhang, "Controllable Swarming and Assembly of Micro/Nanomachines," *Micromachines*, vol. 9, no. 1, p. 10, Dec. 2017, doi: 10.3390/mi9010010.

[17] N. K. Jain, V. Mishra, and N. K. Mehra, "Targeted drug delivery to macrophages," *Expert Opin. Drug Deliv.*, vol. 10, no. 3, pp. 353–367, Mar. 2013, doi: 10.1517/17425247.2013.751370.

[18] S. Zannella, "Biological Effects of Magnetic Fields".

[19] M. P. Kummer, J. J. Abbott, B. E. Kratochvil, R. Borer, A. Sengul, and B. J. Nelson, "OctoMag: An Electromagnetic System for 5-DOF Wireless Micromanipulation," *IEEE Trans. Robot.*, vol. 26, no. 6, pp. 1006–1017, Dec. 2010, doi: 10.1109/TRO.2010.2073030.

[20] S. Jeong *et al.*, “Penetration of an artificial arterial thromboembolism in a live animal using an intravascular therapeutic microrobot system,” *Med. Eng. Phys.*, vol. 38, no. 4, pp. 403–410, Apr. 2016, doi: 10.1016/j.medengphy.2016.01.001.

[21] H. Keller *et al.*, “Method for navigation and control of a magnetically guided capsule endoscope in the human stomach,” in *2012 4th IEEE RAS & EMBS International Conference on Biomedical Robotics and Biomechatronics (BioRob)*, Rome, Italy: IEEE, Jun. 2012, pp. 859–865. Accessed: Dec. 19, 2019. [Online]. Available: http://ieeexplore.ieee.org/document/6290795/

[22] F. Qiu *et al.*, “Bio-inspired microrobots,” *Mater. Today*, vol. 15, no. 10, p. 463, Oct. 2012, doi: 10.1016/S1369-7021(12)70201-8.

[23] S. Kim, S. Lee, J. Lee, B. J. Nelson, L. Zhang, and H. Choi, “Fabrication and Manipulation of Ciliary Microrobots with Non-reciprocal Magnetic Actuation,” *Sci. Rep.*, vol. 6, no. 1, Art. no. 1, Jul. 2016, doi: 10.1038/srep30713.

[24] T. Li *et al.*, “Magnetically Propelled Fish-Like Nanoswimmers,” *Small*, vol. 12, no. 44, pp. 6098–6105, Nov. 2016, doi: 10.1002/smll.201601846.

[25] B. Jang *et al.*, “Undulatory Locomotion of Magnetic Multilink Nanoswimmers,” *Nano Lett.*, vol. 15, no. 7, pp. 4829–4833, Jul. 2015, doi: 10.1021/acs.nanolett.5b01981.

[26] Z. Wu *et al.*, “A swarm of slippery micropropellers penetrates the vitreous body of the eye,” *Sci. Adv.*, vol. 4, no. 11, p. eaat4388, Nov. 2018, doi: 10.1126/sciadv.aat4388.

[27] S. Tottori, L. Zhang, F. Qiu, K. K. Krawczyk, A. Franco-Obregón, and Bradley J. Nelson, “Magnetic Helical Micromachines: Fabrication, Controlled Swimming, and Cargo Transport,” *Adv. Mater.*, vol. 24, no. 6, pp. 811–816, Feb. 2012, doi: 10.1002/adma.201103818.

[28] A. Servant, F. Qiu, M. Mazza, K. Kostarelos, and B. J. Nelson, “Controlled In Vivo Swimming of a Swarm of Bacteria-Like Microrobotic Flagella,” *Adv. Mater.*, vol. 27, no. 19, pp. 2981–2988, May 2015, doi: 10.1002/adma.201404444.

[29] U. Bozuyuk, A. Aghakhani, Y. Alapan, M. Yunusa, P. Wrede, and M. Sitti, “Reduced rotational flows enable the translation of surface-rolling microrobots in confined spaces,” *Nat. Commun.*, vol. 13, no. 1, p. 6289, Oct. 2022, doi: 10.1038/s41467-022-34023-z.

[30] Y. Gao, B. Sprinkle, E. Springer, D. W. M. Marr, and N. Wu, “Rolling of soft microbots with tunable traction,” *Sci. Adv.*, vol. 9, no. 16, p. eadg0919, Apr. 2023, doi: 10.1126/sciadv.adg0919.

[31] D. Disharoon, K. B. Neeves, and D. W. M. Marr, “ac/dc Magnetic Fields for Enhanced Translation of Colloidal Microwheels,” *Langmuir*, vol. 35, no. 9, pp. 3455–3460, Mar. 2019, doi: 10.1021/acs.langmuir.8b04084.

[32] G. Helgesen, “Propulsion of microspheres in fluids using rotating magnetic fields,” *Eur. Phys. J. Spec. Top.*, vol. 227, no. 17, pp. 2425–2438, Mar. 2019, doi: 10.1140/epjst/e2019-800041-3.

[33] H. Xie *et al.*, “Reconfigurable magnetic microrobot swarm: multimode transformation, locomotion, and manipulation,” *Sci. Robot.*, vol. 4, no. 28, p. eaav8006, Mar. 2019, doi: 10.1126/scirobotics.aav8006.

[34] D. Gong *et al.*, “Controlled propulsion of wheel-shape flaky microswimmers under rotating magnetic fields,” *Appl. Phys. Lett.*, vol. 114, no. 12, p. 123701, Mar. 2019, doi: 10.1063/1.5090297.

[35] S. Yu *et al.*, “Self-Propelled Janus Microdimer Swimmers under a Rotating Magnetic Field,” *Nanomaterials*, vol. 9, no. 12, p. 1672, Nov. 2019, doi: 10.3390/nano9121672.

[36] T. O. Tasci, P. S. Herson, K. B. Neeves, and D. W. M. Marr, “Surface-enabled propulsion and control of colloidal microwheels,” *Nat. Commun.*, vol. 7, p. 10225, Jan. 2016, doi: 10.1038/ncomms10225.

[37] T. Yang, A. Tomaka, T. O. Tasci, K. B. Neeves, N. Wu, and D. W. M. Marr, "Microwheels on microroads: Enhanced translation on topographic surfaces," *Sci. Robot.*, vol. 4, no. 32, p. eaaw9525, Jul. 2019, doi: 10.1126/scirobotics.aaw9525.

[38] H. Chen, W. Kreider, A. A. Brayman, M. R. Bailey, and T. J. Matula, "Blood Vessel Deformations on Microsecond Time Scales by Ultrasonic Cavitation," *Phys. Rev. Lett.*, vol. 106, no. 3, p. 034301, Jan. 2011, doi: 10.1103/PhysRevLett.106.034301.

[39] H. Ceylan, I. C. Yasa, U. Kilic, W. Hu, and M. Sitti, "Translational prospects of untethered medical microrobots," *Prog. Biomed. Eng.*, vol. 1, no. 1, p. 012002, Jul. 2019, doi: 10.1088/2516-1091/ab22d5.

[40] J. J. Abbott, E. Diller, and A. J. Petruska, "Magnetic Methods in Robotics," *Annu. Rev. Control Robot. Auton. Syst.*, vol. 3, no. 1, p. annurev-control-081219-082713, May 2020, doi: 10.1146/annurev-control-081219-082713.

[41] J. Rahmer, C. Stehning, and B. Gleich, "Spatially selective remote magnetic actuation of identical helical micromachines," *Sci. Robot.*, vol. 2, no. 3, p. eaal2845, Feb. 2017, doi: 10.1126/scirobotics.aal2845.

[42] A. W. Mahoney, J. C. Sarrazin, E. Bamberg, and J. J. Abbott, "Velocity Control with Gravity Compensation for Magnetic Helical Microswimmers," *Adv. Robot.*, vol. 25, no. 8, pp. 1007–1028, Jan. 2011, doi: 10.1163/016918611X568620.

[43] G. Helgesen, "Magnetic propulsion of microspheres at liquid-glass interfaces," *J. Appl. Phys.*, vol. 123, no. 6, p. 064902, Feb. 2018, doi: 10.1063/1.5011350.

[44] S. Lee *et al.*, "A Needle-Type Microrobot for Targeted Drug Delivery by Affixing to a Microtissue," *Adv. Healthc. Mater.*, p. 1901697, Mar. 2020.

[45] Y.-L. Liu, D. Chen, P. Shang, and D.-C. Yin, "A review of magnet systems for targeted drug delivery," *J. Controlled Release*, vol. 302, pp. 90–104, May 2019, doi: 10.1016/j.jconrel.2019.03.031.

[46] A. J. Petruska and B. J. Nelson, "Minimum Bounds on the Number of Electromagnets Required for Remote Magnetic Manipulation," *IEEE Trans. Robot.*, vol. 31, no. 3, pp. 714–722, Jun. 2015, doi: 10.1109/TRO.2015.2424051.

[47] E. Diller, J. Giltinan, G. Zhan Lum, Z. Ye, and M. Sitti, "Six-Degrees-of-Freedom Remote Actuation of Magnetic Microrobots," in *Robotics: Science and Systems X*, Robotics: Science and Systems Foundation, Jul. 2014. Accessed: Sep. 09, 2019. [Online]. Available: http://www.roboticsproceedings.org/rss10/p13.pdf

[48] B. E. Kratochvil *et al.*, "MiniMag: A Hemispherical Electromagnetic System for 5-DOF Wireless Micromanipulation," in *Experimental Robotics*, O. Khatib, V. Kumar, and G. Sukhatme, Eds., Berlin, Heidelberg: Springer Berlin Heidelberg, 2014, pp. 317–329. doi: 10.1007/978-3-642-28572-1_22.

[49] A. Pourkand and J. J. Abbott, "A Critical Analysis of Eight-Electromagnet Manipulation Systems: The Role of Electromagnet Configuration on Strength, Isotropy, and Access," *IEEE Robot. Autom. Lett.*, vol. 3, no. 4, pp. 2957–2962, Oct. 2018, doi: 10.1109/LRA.2018.2846800.

[50] P. Berkelman and M. Dzadovsky, "Magnetic Levitation Over Large Translation and Rotation Ranges in All Directions," *IEEEASME Trans. Mechatron.*, vol. 18, no. 1, pp. 44–52, Feb. 2013, doi: 10.1109/TMECH.2011.2161614.

[51] E. S. Gang *et al.*, "Dynamically Shaped Magnetic Fields: Initial Animal Validation of a New Remote Electrophysiology Catheter Guidance and Control System," *Circ. Arrhythm. Electrophysiol.*, vol. 4, no. 5, pp. 770–777, Oct. 2011, doi: 10.1161/CIRCEP.110.959692.

[52] A. J. Petruska and J. J. Abbott, "Omnimagnet: An Omnidirectional Electromagnet for Controlled Dipole-Field Generation," *IEEE Trans. Magn.*, vol. 50, no. 7, pp. 1–10, Jul. 2014, doi: 10.1109/TMAG.2014.2303784.

[53] J. J. Abbott and B. Osting, "Optimization of Coreless Electromagnets to Maximize Field Generation for Magnetic Manipulation Systems," *IEEE Magn. Lett.*, vol. 9, pp. 1–4, 2018, doi: 10.1109/LMAG.2017.2768021.

[54] A. W. Mahoney and J. J. Abbott, "Generating Rotating Magnetic Fields With a Single Permanent Magnet for Propulsion of Untethered Magnetic Devices in a Lumen," *IEEE Trans. Robot.*, vol. 30, no. 2, pp. 411–420, Apr. 2014, doi: 10.1109/TRO.2013.2289019.

[55] S. E. Wright, A. W. Mahoney, K. M. Popek, and J. J. Abbott, "The Spherical-Actuator-Magnet Manipulator: A Permanent-Magnet Robotic End-Effector," *IEEE Trans. Robot.*, vol. 33, no. 5, pp. 1013–1024, Oct. 2017, doi: 10.1109/TRO.2017.2694841.

[56] P. F. Costa *et al.*, "Mimicking arterial thrombosis in a 3D-printed microfluidic in vitro vascular model based on computed tomography angiography data," *Lab. Chip*, vol. 17, no. 16, pp. 2785–2792, 2017, doi: 10.1039/C7LC00202E.

[57] V. Saggiomo and A. H. Velders, "Simple 3D Printed Scaffold-Removal Method for the Fabrication of Intricate Microfluidic Devices," *Adv. Sci.*, vol. 2, no. 9, p. 1500125, Sep. 2015, doi: 10.1002/advs.201500125.

[58] O. Jeon, Y. B. Lee, H. Jeong, S. J. Lee, D. Wells, and E. Alsberg, "Individual cell-only bioink and photocurable supporting medium for 3D printing and generation of engineered tissues with complex geometries," *Mater. Horiz.*, vol. 6, no. 8, pp. 1625–1631, Sep. 2019, doi: 10.1039/C9MH00375D.

[59] B. Grigoryan *et al.*, "Multivascular networks and functional intravascular topologies within biocompatible hydrogels," *Science*, vol. 364, no. 6439, pp. 458–464, May 2019, doi: 10.1126/science.aav9750.

[60] J. Li, C. Wu, P. K. Chu, and M. Gelinsky, "3D printing of hydrogels: Rational design strategies and emerging biomedical applications," *Mater. Sci. Eng. R Rep.*, vol. 140, p. 100543, Apr. 2020, doi: 10.1016/j.mser.2020.100543.

[61] Y. S. Lui, W. T. Sow, L. P. Tan, Y. Wu, Y. Lai, and H. Li, "4D printing and stimuli-responsive materials in biomedical aspects," *Acta Biomater.*, vol. 92, pp. 19–36, Jul. 2019, doi: 10.1016/j.actbio.2019.05.005.

[62] J. Choi, J. Hwang, J. Kim, and H. Choi, "Recent Progress in Magnetically Actuated Microrobots for Targeted Delivery of Therapeutic Agents," *Adv. Healthc. Mater.*, vol. 10, no. 6, p. 2001596, Mar. 2021, doi: 10.1002/adhm.202001596.

[63] X.-Z. Chen *et al.*, "Hybrid Magnetoelectric Nanowires for Nanorobotic Applications: Fabrication, Magnetoelectric Coupling, and Magnetically Assisted In Vitro Targeted Drug Delivery," *Adv. Mater.*, vol. 29, no. 8, p. 1605458, Feb. 2017, doi: 10.1002/adma.201605458.

[64] T. Yang *et al.*, "Reconfigurable microbots folded from simple colloidal chains," *Proc. Natl. Acad. Sci.*, p. 202007255, Jul. 2020, doi: 10.1073/pnas.2007255117.

[65] Y. Alapan, U. Bozuyuk, P. Erkoc, A. C. Karacakol, and M. Sitti, "Multifunctional surface microrollers for targeted cargo delivery in physiological blood flow," *Sci. Robot.*, vol. 5, no. 42, p. eaba5726, May 2020, doi: 10.1126/scirobotics.aba5726.

[66] Y. Yang and Y. Zhao, "Discretized Motion of Surface Walker under a Nonuniform AC Magnetic Field," *Langmuir*, vol. 36, no. 37, pp. 11125–11137, Sep. 2020, doi: 10.1021/acs.langmuir.0c02132.

[67] J. Vyskočil, C. C. Mayorga-Martinez, E. Jablonská, F. Novotný, T. Ruml, and M. Pumera, "Cancer Cells Microsurgery *via* Asymmetric Bent Surface Au/Ag/Ni Microrobotic Scalpels Through a

Transversal Rotating Magnetic Field," *ACS Nano*, vol. 14, no. 7, pp. 8247–8256, Jul. 2020, doi: 10.1021/acsnano.0c01705.

[68] G. Hwang *et al.*, "Catalytic antimicrobial robots for biofilm eradication," *Sci. Robot.*, vol. 4, no. 29, p. eaaw2388, Apr. 2019, doi: 10.1126/scirobotics.aaw2388.

[69] U. Bozuyuk, Y. Alapan, A. Aghakhani, M. Yunusa, and M. Sitti, "Shape anisotropy-governed locomotion of surface microrollers on vessel-like microtopographies against physiological flows," *Proc. Natl. Acad. Sci.*, vol. 118, no. 13, p. e2022090118, Mar. 2021, doi: 10.1073/pnas.2022090118.

[70] D. Ahmed, D. Hauri, A. Sukhov, D. Rodrigue, M. Gian, and B. Nelson, "Bio-inspired Acousto-magnetic Microswarm Robots with Upstream Motility," *Nat. Mach. Intell.*, vol. 3, pp. 116–124, 2021, doi: https://doi.org/10.1038/s42256-020-00275-x.

[71] H. Zhou, C. C. Mayorga-Martinez, S. Pané, L. Zhang, and M. Pumera, "Magnetically Driven Micro and Nanorobots," *Chem. Rev.*, vol. 121, no. 8, pp. 4999–5041, Apr. 2021, doi: 10.1021/acs.chemrev.0c01234.

[72] L. Yang and L. Zhang, "Motion Control in Magnetic Microrobotics: From Individual and Multiple Robots to Swarms," *Annu. Rev. Control Robot. Auton. Syst.*, vol. 4, no. 1, pp. 509–534, 2021, doi: 10.1146/annurev-control-032720-104318.

[73] J. Yu, L. Yang, and L. Zhang, "Pattern generation and motion control of a vortex-like paramagnetic nanoparticle swarm," *Int. J. Robot. Res.*, vol. 37, no. 8, p. 19, 2018, doi: https://doi.org/10.1177/0278364918784366.

[74] G. Kokot and A. Snezhko, "Manipulation of emergent vortices in swarms of magnetic rollers," *Nat. Commun.*, vol. 9, no. 1, p. 2344, Dec. 2018, doi: 10.1038/s41467-018-04765-w.

[75] J. Yu, B. Wang, X. Du, Q. Wang, and L. Zhang, "Ultra-extensible ribbon-like magnetic microswarm," *Nat. Commun.*, vol. 9, no. 1, p. 3260, Dec. 2018, doi: 10.1038/s41467-018-05749-6.

[76] F. Martinez-Pedrero and P. Tierno, "Magnetic Propulsion of Self-Assembled Colloidal Carpets: Efficient Cargo Transport via a Conveyor-Belt Effect," *Phys. Rev. Appl.*, vol. 3, no. 5, p. 051003, May 2015, doi: 10.1103/PhysRevApplied.3.051003.

[77] B. Yigit, Y. Alapan, and M. Sitti, "Programmable Collective Behavior in Dynamically Self-Assembled Mobile Microrobotic Swarms," *Adv. Sci.*, vol. 6, no. 6, p. 1801837, Mar. 2019, doi: 10.1002/advs.201801837.

[78] Q. Wang, J. Yu, K. Yuan, L. Yang, D. Jin, and L. Zhang, "Disassembly and spreading of magnetic nanoparticle clusters on uneven surfaces," *Appl. Mater. Today*, vol. 18, p. 100489, Mar. 2020, doi: 10.1016/j.apmt.2019.100489.

[79] B. Wang *et al.*, "Reconfigurable Swarms of Ferromagnetic Colloids for Enhanced Local Hyperthermia," *Adv. Funct. Mater.*, vol. 28, no. 25, p. 1705701, Jun. 2018, doi: 10.1002/adfm.201705701.

[80] J. Yu, D. Jin, K.-F. Chan, Q. Wang, K. Yuan, and L. Zhang, "Active generation and magnetic actuation of microrobotic swarms in bio-fluids," *Nat. Commun.*, vol. 10, no. 1, p. 5631, Dec. 2019, doi: 10.1038/s41467-019-13576-6.

[81] T.-Y. Huang *et al.*, "3D Printed Microtransporters: Compound Micromachines for Spatiotemporally Controlled Delivery of Therapeutic Agents," *Adv. Mater.*, vol. 27, no. 42, pp. 6644–6650, Nov. 2015, doi: 10.1002/adma.201503095.

[82] G. Chatzipirpiridis *et al.*, "Template-Assisted Electroforming of Fully Semi-Hard-Magnetic Helical Microactuators," *Adv. Eng. Mater.*, vol. 20, no. 9, p. 1800179, Sep. 2018, doi: 10.1002/adem.201800179.

[83] A. Barbot, D. Decanini, and G. Hwang, "The Rotation of Microrobot Simplifies 3D Control Inside Microchannels," *Sci. Rep.*, vol. 8, no. 1, Dec. 2018, doi: 10.1038/s41598-017-18891-w.

[84] K. M. Bratlie, T. T. Dang, S. Lyle, M. Nahrendorf, R. Weissleder, and D. G. Anderson, "Rapid Biocompatibility Analysis of Materials via In Vivo Fluorescence Imaging of Mouse Models," *PLoS ONE*, vol. 5, no. 4, p. 8, 2010.

[85] K. Makino, N. Yamamoto, K. Higuchi, N. Harada, H. Ohshima, and H. Terada, "Phagocytic uptake of polystyrene microspheres by alveolar macrophages: effects of the size and surface properties of the microspheres," *Colloids Surf. B Biointerfaces*, vol. 27, no. 1, pp. 33–39, Jan. 2003, doi: 10.1016/S0927-7765(02)00042-5.

[86] F. J. Maier *et al.*, "Non reciprocal skewed rolling of a colloidal wheel due to induced chirality," *Soft Matter*, vol. 12, no. 46, pp. 9314–9320, 2016, doi: 10.1039/C6SM02143C.

[87] G. B. Jeffery, "On the Steady Rotation of a Solid of Revolution in a Viscous Fluid," *Proc. Lond. Math. Soc.*, vol. s2_14, no. 1, pp. 327–338, 1915, doi: 10.1112/plms/s2_14.1.327.

[88] D. J. Klingenberg, J. C. Ulicny, and M. A. Golden, "Mason numbers for magnetorheology," *J. Rheol.*, vol. 51, no. 5, pp. 883–893, Sep. 2007, doi: 10.1122/1.2764089.

[89] S. L. Biswal and A. P. Gast, "Rotational dynamics of semiflexible paramagnetic particle chains," *Phys. Rev. E*, vol. 69, no. 4, p. 041406, Apr. 2004, doi: 10.1103/PhysRevE.69.041406.

[90] E. S. Lein *et al.*, "Genome-wide atlas of gene expression in the adult mouse brain," *Nature*, vol. 445, no. 7124, pp. 168–176, Jan. 2007, doi: 10.1038/nature05453.

[91] B. Xiong *et al.*, "Precise Cerebral Vascular Atlas in Stereotaxic Coordinates of Whole Mouse Brain," *Front. Neuroanat.*, vol. 11, p. 128, Dec. 2017, doi: 10.3389/fnana.2017.00128.

[92] S. Upadhyayula *et al.*, "Coatings of Polyethylene Glycol for Suppressing Adhesion between Solid Microspheres and Flat Surfaces," *Langmuir*, vol. 28, no. 11, pp. 5059–5069, Mar. 2012, doi: 10.1021/la300545v.

[93] M. B. Gorbet and M. V. Sefton, "Complement inhibition reduces material-induced leukocyte activation with PEG modified polystyrene beads (Tentagel^{TM}) but not polystyrene beads," *J. Biomed. Mater. Res. A*, vol. 74A, no. 4, pp. 511–522, Sep. 2005, doi: 10.1002/jbm.a.30354.

[94] N. Nishimura, C. B. Schaffer, B. Friedman, P. S. Tsai, P. D. Lyden, and D. Kleinfeld, "Targeted insult to subsurface cortical blood vessels using ultrashort laser pulses: three models of stroke," *Nat. Methods*, vol. 3, no. 2, pp. 99–108, Feb. 2006, doi: 10.1038/nmeth844.

[95] J. Chen and Y. Wang, "Personalized dynamic transport of magnetic nanorobots inside the brain vasculature," *Nanotechnology*, vol. 31, no. 49, p. 495706, Dec. 2020, doi: 10.1088/1361-6528/abb392.

[96] E. Roth, C. J. Zimmermann, D. Disharoon, T. O. Tasci, D. W. M. Marr, and K. B. Neeves, "An experimental design for the control and assembly of superparamagnetic μwheels," *Rev. Sci. Instrum.*, 2020.

[97] "GitHub - czimm79," *GitHub*. https://github.com/czimm79

[98] D. B. Allan, T. Caswell, N. C. Keim, and C. M. van der Wel, "trackpy: Trackpy v0.4.1." Zenodo, Apr. 2018. doi: 10.5281/zenodo.1226458.

[99] J. Schindelin *et al.*, "Fiji: an open-source platform for biological-image analysis," *Nat. Methods*, vol. 9, no. 7, pp. 676–682, Jul. 2012, doi: 10.1038/nmeth.2019.

[100] C. Zimmermann, "czimm79/mutracker: v1.0.1." Zenodo, Dec. 2021. doi: 10.5281/zenodo.5793894.

[101] W. B. Russel, D. A. Saville, and W. R. Schowalter, *Colloidal Dispersions*. Cambridge University Press, 1989.

[102] Yorisaburo Takaisi, "Note on the Drag on a Circular Cylinder moving with Low Speeds in a Semi-Infinite Viscous Liquid bounded by a Plane Wall," *J. Phys. Soc. Jpn.*, vol. 11, no. 9, Sep. 1956.

[103] Y. Dong *et al.*, "Endoscope-assisted magnetic helical micromachine delivery for biofilm eradication in tympanostomy tube," *Sci. Adv.*, vol. 8, no. 40, p. eabq8573, Oct. 2022, doi: 10.1126/sciadv.abq8573.

[104] Q. Wang, X. Du, D. Jin, and L. Zhang, "Real-Time Ultrasound Doppler Tracking and Autonomous Navigation of a Miniature Helical Robot for Accelerating Thrombolysis in Dynamic Blood Flow," *ACS Nano*, vol. 16, no. 1, pp. 604–616, Jan. 2022, doi: 10.1021/acsnano.1c07830.

[105] M. B. Akolpoglu *et al.*, "Magnetically steerable bacterial microrobots moving in 3D biological matrices for stimuli-responsive cargo delivery," *Sci. Adv.*, vol. 8, no. 28, p. eabo6163, Jul. 2022, doi: 10.1126/sciadv.abo6163.

[106] D. Liu, T. Wang, and Y. Lu, "Untethered Microrobots for Active Drug Delivery: From Rational Design to Clinical Settings," *Adv. Healthc. Mater.*, vol. 11, no. 3, p. 2102253, Feb. 2022, doi: 10.1002/adhm.202102253.

[107] D. Disharoon, B. G. Trewyn, P. S. Herson, D. W. M. Marr, and K. B. Neeves, "Breaking the fibrinolytic speed limit with microwheel co-delivery of tissue plasminogen activator and plasminogen," *J. Thromb. Haemost.*, vol. 20, no. 2, pp. 486–497, 2022, doi: https://doi.org/10.1111/jth.15617.

[108] T. Maric *et al.*, "Microrobots Derived from Variety Plant Pollen Grains for Efficient Environmental Clean Up and as an Anti-Cancer Drug Carrier," *Adv. Funct. Mater.*, vol. 30, no. 19, p. 2000112, 2020, doi: 10.1002/adfm.202000112.

[109] J. Park, C. Jin, S. Lee, J. Kim, and H. Choi, "Magnetically Actuated Degradable Microrobots for Actively Controlled Drug Release and Hyperthermia Therapy," *Adv. Healthc. Mater.*, vol. 8, no. 16, p. 1900213, Aug. 2019, doi: 10.1002/adhm.201900213.

[110] S. Noh *et al.*, "A Biodegradable Magnetic Microrobot Based on Gelatin Methacrylate for Precise Delivery of Stem Cells with Mass Production Capability," *Small*, vol. 18, no. 25, p. 2107888, 2022, doi: 10.1002/smll.202107888.

[111] R. Sanchis-Gual *et al.*, "3D Printed Template-Assisted Casting of Biocompatible Polyvinyl Alcohol-Based Soft Microswimmers with Tunable Stability," *Adv. Funct. Mater.*, vol. n/a, no. n/a, p. 2212952, doi: 10.1002/adfm.202212952.

[112] L. Yang, J. Yu, S. Yang, B. Wang, B. J. Nelson, and L. Zhang, "A Survey on Swarm Microrobotics," *IEEE Trans. Robot.*, vol. 38, no. 3, pp. 1531–1551, Jun. 2022, doi: 10.1109/TRO.2021.3111788.

[113] G. Gardi, S. Ceron, W. Wang, K. Petersen, and M. Sitti, "Microrobot collectives with reconfigurable morphologies, behaviors, and functions," *Nat. Commun.*, vol. 13, no. 1, p. 2239, Dec. 2022, doi: 10.1038/s41467-022-29882-5.

[114] C. J. Zimmermann, P. S. Herson, K. B. Neeves, and D. W. M. Marr, "Multimodal microwheel swarms for targeting in three-dimensional networks," *Sci. Rep.*, vol. 12, no. 1, p. 5078, Dec. 2022, doi: 10.1038/s41598-022-09177-x.

[115] D. Li, Y. Liu, Y. Yang, and Y. Shen, "A fast and powerful swimming microrobot with a serrated tail enhanced propulsion interface," *Nanoscale*, vol. 10, no. 42, pp. 19673–19677, 2018, doi: 10.1039/C8NR04907F.

[116] L. Dekanovsky, B. Khezri, Z. Rottnerova, F. Novotny, J. Plutnar, and M. Pumera, “Chemically programmable microrobots weaving a web from hormones,” *Nat. Mach. Intell.*, vol. 2, no. 11, pp. 711–718, Nov. 2020, doi: 10.1038/s42256-020-00248-0.

[117] V. Sridhar *et al.*, “Light-driven carbon nitride microswimmers with propulsion in biological and ionic media and responsive on-demand drug delivery,” *Sci. Robot.*, vol. 7, no. 62, p. eabm1421, Jan. 2022, doi: 10.1126/scirobotics.abm1421.

[118] M. Urso, M. Ussia, F. Novotný, and M. Pumera, “Trapping and detecting nanoplastics by MXene-derived oxide microrobots,” *Nat. Commun.*, vol. 13, no. 1, p. 3573, Jun. 2022, doi: 10.1038/s41467-022-31161-2.

[119] F. Ji, D. Jin, B. Wang, and L. Zhang, “Light-Driven Hovering of a Magnetic Microswarm in Fluid,” *ACS Nano*, p. 9, 2020.

[120] J. F. Schenck, “Safety of Strong, Static Magnetic Fields,” p. 18.

[121] N. B. Day, W. C. Wixson, and C. W. Shields, “Magnetic systems for cancer immunotherapy,” *Acta Pharm. Sin. B*, vol. 11, no. 8, pp. 2172–2196, Aug. 2021, doi: 10.1016/j.apsb.2021.03.023.

[122] W. Xi, A. A. Solovev, A. N. Ananth, D. H. Gracias, S. Sanchez, and O. G. Schmidt, “Rolled-up magnetic microdrillers: towards remotely controlled minimally invasive surgery,” *Nanoscale*, vol. 5, no. 4, pp. 1294–1297, Feb. 2013, doi: 10.1039/c2nr32798h.

[123] E. Kim *et al.*, “A magnetically actuated microrobot for targeted neural cell delivery and selective connection of neural networks,” *Sci. Adv.*, vol. 6, no. 39, p. eabb5696, Sep. 2020, doi: 10.1126/sciadv.abb5696.

[124] Y. Chen *et al.*, “Carbon Helical Nanorobots Capable of Cell Membrane Penetration for Single Cell Targeted SERS Bio-Sensing and Photothermal Cancer Therapy,” *Adv. Funct. Mater.*, vol. 32, no. 30, p. 2200600, 2022, doi: 10.1002/adfm.202200600.

[125] K.-W. Gyak *et al.*, “Magnetically Actuated SiCN-Based Ceramic Microrobot for Guided Cell Delivery,” *Adv. Healthc. Mater.*, vol. 8, no. 21, p. 1900739, 2019, doi: 10.1002/adhm.201900739.

[126] Y. Dong, L. Wang, V. Iacovacci, X. Wang, L. Zhang, and B. J. Nelson, “Magnetic helical micro-/nanomachines: Recent progress and perspective,” *Matter*, vol. 5, no. 1, pp. 77–109, Jan. 2022, doi: 10.1016/j.matt.2021.10.010.

[127] C. J. Zimmermann, T. Schraeder, B. Reynolds, E. M. DeBoer, K. B. Neeves, and D. W. M. Marr, “Delivery and actuation of aerosolized microbots,” *Nano Sel.*, p. nano.202100353, Mar. 2022, doi: 10.1002/nano.202100353.

[128] J. Hwang, J. Kim, and H. Choi, “A review of magnetic actuation systems and magnetically actuated guidewire- and catheter-based microrobots for vascular interventions,” *Intell. Serv. Robot.*, vol. 13, no. 1, pp. 1–14, Jan. 2020, doi: 10.1007/s11370-020-00311-0.

[129] A. W. Mahoney and J. J. Abbott, “Managing magnetic force applied to a magnetic device by a rotating dipole field,” *Appl. Phys. Lett.*, vol. 99, no. 13, p. 134103, Sep. 2011, doi: 10.1063/1.3644021.

[130] A. Spatafora-Salazar, D. M. Lobmeyer, L. H. P. Cunha, K. Joshi, and S. L. Biswal, “Hierarchical assemblies of superparamagnetic colloids in time-varying magnetic fields,” *Soft Matter*, vol. 17, no. 5, pp. 1120–1155, 2021, doi: 10.1039/D0SM01878C.

[131] M. K. D. Manshadi *et al.*, “Magnetic aerosol drug targeting in lung cancer therapy using permanent magnet,” *Drug Deliv.*, vol. 26, no. 1, pp. 120–128, Jan. 2019, doi: 10.1080/10717544.2018.1561765.

[132] C. Bor Fuh and S. Y. Chen, “Magnetic split-flow thin fractionation: new technique for separation of magnetically susceptible particles,” *J. Chromatogr. A*, vol. 813, no. 2, pp. 313–324, Jul. 1998, doi: 10.1016/S0021-9673(98)00337-9.

[133] C. E. Sing, L. Schmid, M. F. Schneider, T. Franke, and A. Alexander-Katz, “Controlled surface-induced flows from the motion of self-assembled colloidal walkers,” *Proc. Natl. Acad. Sci.*, vol. 107, no. 2, pp. 535–540, Jan. 2010, doi: 10.1073/pnas.0906489107.

[134] B. Chaluvadi, K. M. Stewart, A. J. Sperry, H. C. Fu, and J. J. Abbott, “Kinematic Model of a Magnetic-Microrobot Swarm in a Rotating Magnetic Dipole Field,” *IEEE Robot. Autom. Lett.*, vol. 5, no. 2, pp. 2419–2426, Apr. 2020, doi: 10.1109/LRA.2020.2972857.

[135] X. Fan *et al.*, “Scale-reconfigurable miniature ferrofluidic robots for negotiating sharply variable spaces,” *Sci. Adv.*, vol. 8, no. 37, p. eabq1677, Sep. 2022, doi: 10.1126/sciadv.abq1677.

[136] G. Fonnum, C. Johansson, A. Molteberg, S. Mørup, and E. Aksnes, “Characterisation of Dynabeads® by magnetization measurements and Mössbauer spectroscopy,” *J. Magn. Magn. Mater.*, vol. 293, no. 1, pp. 41–47, May 2005, doi: 10.1016/j.jmmm.2005.01.041.

[137] J. Bezanson, A. Edelman, S. Karpinski, and V. B. Shah, “Julia: A Fresh Approach to Numerical Computing,” *SIAM Rev.*, vol. 59, no. 1, pp. 65–98, Jan. 2017, doi: 10.1137/141000671.

[138] C. A. Schneider, W. S. Rasband, and K. W. Eliceiri, “NIH Image to ImageJ: 25 years of image analysis,” *Nat. Methods*, vol. 9, no. 7, Art. no. 7, Jul. 2012, doi: 10.1038/nmeth.2089.

[139] J. C. Crocker and D. G. Grier, “Methods of Digital Video Microscopy for Colloidal Studies,” *J. Colloid Interface Sci.*, vol. 179, no. 1, pp. 298–310, Apr. 1996, doi: 10.1006/jcis.1996.0217.

[140] D. B. Allan, T. Caswell, N. C. Keim, C. M. van der Wel, and R. W. Verweij, “soft-matter/trackpy: v0.6.1.” Zenodo, Feb. 2023. doi: 10.5281/zenodo.7670439.

[141] S. Danisch and J. Krumbiegel, “Makie.jl: Flexible high-performance data visualization for Julia,” *J. Open Source Softw.*, vol. 6, no. 65, p. 3349, 2021, doi: 10.21105/joss.03349.

[142] J.-Y. Tinevez *et al.*, “TrackMate: An open and extensible platform for single-particle tracking,” *Methods*, vol. 115, pp. 80–90, 2017, doi: https://doi.org/10.1016/j.ymeth.2016.09.016.

[143] F. van der Plas *et al.*, “fonsp/Pluto.jl: v0.18.1.” Zenodo, Feb. 2022. doi: 10.5281/zenodo.6234110.

[144] M. J. Osmond, E. Korthals, C. J. Zimmermann, E. J. Roth, D. W. M. Marr, and K. B. Neeves, “Magnetically Powered Chitosan Milliwheels for Rapid Translation, Barrier Function Rescue, and Delivery of Therapeutic Proteins to the Inflamed Gut Epithelium,” *ACS Omega*, vol. 8, no. 12, pp. 11614–11622, Mar. 2023, doi: 10.1021/acsomega.3c00886.

[145] E. Wolvington, L. Yeager, Y. Gao, C. J. Zimmermann, and D. W. M. Marr, “Paddlebots: Translation of Rotating Colloidal Assemblies near an Air/Water Interface,” *Langmuir*, vol. 39, no. 22, pp. 7846–7851, Jun. 2023, doi: 10.1021/acs.langmuir.3c00701.

[146] A. F. Smith *et al.*, “Brain Capillary Networks Across Species: A few Simple Organizational Requirements Are Sufficient to Reproduce Both Structure and Function,” *Front. Physiol.*, vol. 10, p. 233, Mar. 2019, doi: 10.3389/fphys.2019.00233.

APPENDIX A SUPPLEMENTARY INFORMATION FOR CHAPTER 2

A.1 Expanded Velocity Expression

$$V(R,\phi) = \frac{R(R^3 mg\delta \sin(\phi) - 16Rmg\delta(R+\delta)^2 G\sin(\phi) + a^3\gamma\eta(-R^2 + 16(R+\delta)^2 G)}{a^3\eta(-R^3 + 16R(R+\delta)^2 G + 128\pi\delta k_2(R+\delta)^2)} \quad \text{(A.1)}$$

where

$$G = \ln\left(\frac{R+\delta}{R} + \ln(2)\right) \quad \text{(A.2)}$$

A.2 Magnetic Field Equations

For all experiments, the circular constant magnitude rotating magnetic field was generated using

$$\omega = 2\pi f \quad \text{(A.3)}$$

$$\mathrm{V}_x = \mathrm{V}_0[\cos(h)\cos(\omega t) - \sin(\theta)\sin(h)\sin(\omega t)]$$

$$\mathrm{V}_y = -\mathrm{V}_0[\sin(h)\cos(\omega t) + \sin(\theta)\cos(h)\sin(\omega t)]$$

$$V_z = C * \mathrm{V}_0\cos(\theta)\sin(\omega t)$$

where V_x, V_y and V_z are voltages applied to each set of coils, V_0 is the voltage multiplier, h the heading angle, θ the camber angle, f the field frequency, t time, and C a coefficient to correct for a different coil distance between the Z coils and the sample compared to the X-Y coils.

A.3 Swarm Actuation Patterns

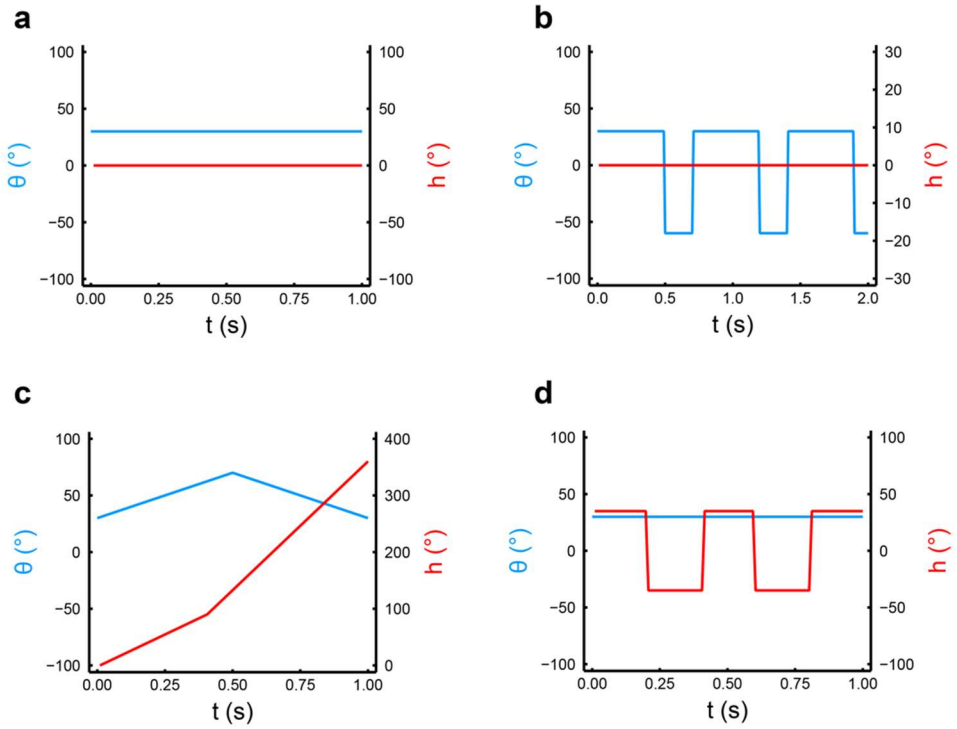

Figure A.1 Actuation patterns for swarm modes. The circular field is modified by changing its heading angle h and camber angle θ in time to create the swarm fields. a) Rolling b) Flipping c) Corkscrew d) Switchback.

A.4 Separation Widths

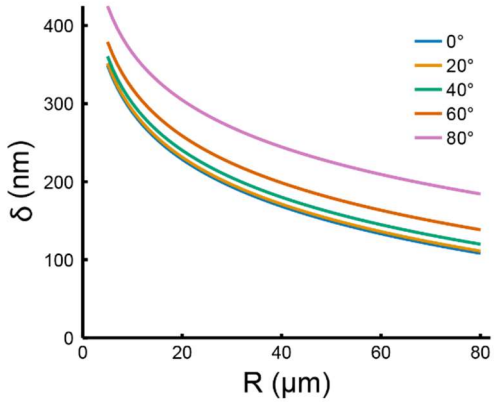

Figure A.2 Calculated μwheel separation widths.

A.5 3D-Printed Model Roughness

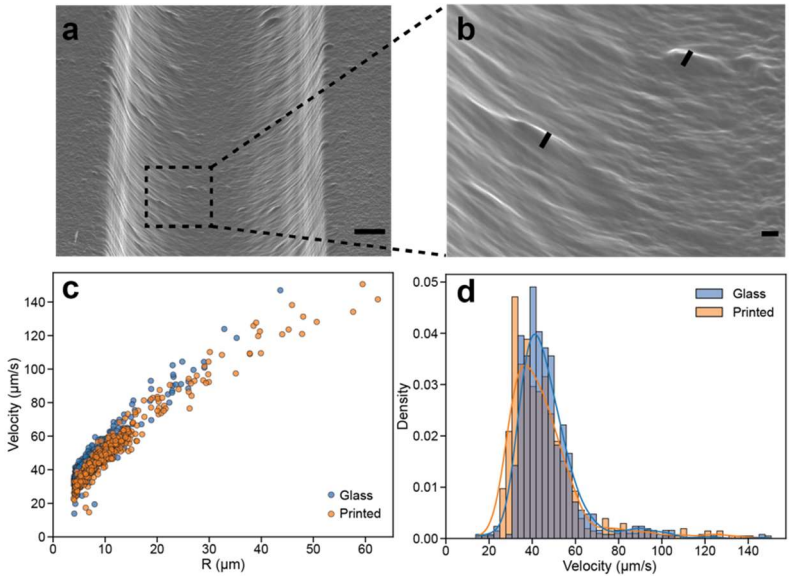

Figure A.3 μWheel travel on 3D printed surfaces a) Scanning electron microscopy of 3D-printed half cylindrical channel. Scale = 100 μm. b) Increased magnification of (a). Scale = 10 μm. c) μWheel velocity on glass and flat 3D-printed surfaces (field = 3.7 mT, 40 Hz, and $\theta = 30°$). d) μWheel velocity probability density distribution.

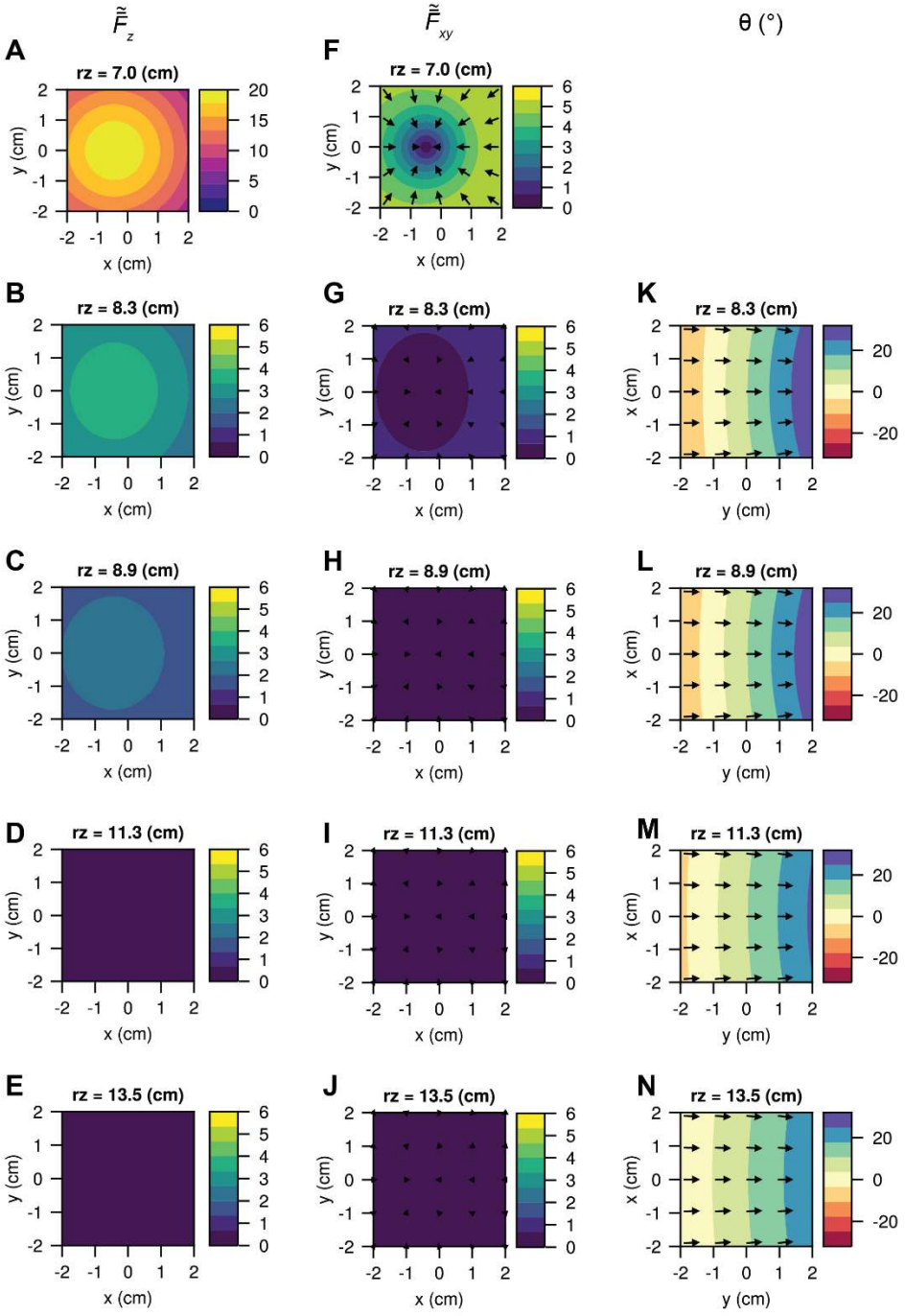

Figure B.4 Simulations of the A-E) force in the z-direction, F-J) force in the xy-direction, and K-N) field angular velocity across a 16 cm^2 working area for all experimental conditions.

APPENDIX C LIST OF ADDITIONAL FILES

C.1 Permissions

Permissions.pdf: Includes all publisher and co-author permissions for reproduced materials.

C.2 Chapter 2

Video 2.SV1: Individual μwheels climbing an 80° incline.

Video 2.SV2: Demonstration of four swarm modes at 0°.

Video 2.SV3: Demonstration of four swarm modes at 65°.

Video 2.SV4: Swarm mode switching inside a 3D printed model to deliver beads at a target region.

C.3 Chapter 3

Video 3.SV1: μWheel translation post aerosolization on a glass surface.

Video 3.SV2. Bead aerosol delivery and wheel assembly on a glass surface (2x speed).

Video 3.SV3. Post aerosolization assembly and translation of

wheels within lung model – distributed mode.

Video 3.SV4. Post aerosolization assembly and translation of wheels within lung model – targeted mode.

C.4 Chapter 4

Video 4.SV1: Directional control of μwheels in the MP-low and MP-assisted modes.

Video 4.SV2. Macro-scale demonstration of all three modes on a μwheel swarm.

Video 4.SV3. Helical maneuver in a cylindrical capillary using MP-low and MP-assisted modes.

Video 4.SV4. Targeting μwheel swarms in a 3D capillary model.